The pyrite multiple sulfur isotope record of the 1.98 Ga Zaonega Formation: evidence for biogeochemical sulfur cycling in a semi-restricted basin

4 K. Paiste[a,*,1], A. Pellerin[b], A. L. Zerkle[c], K. Kirsimäe[d], A. R. Prave[c], A. E. Romashkin[e], A.

5 Lepland[a,d,f]

6 [a]CAGE—Centre for Arctic Gas Hydrate, Environment and Climate, Department of
7 Geosciences, UiT The Arctic University of Norway, 9037 Tromsø, Norway.
8 [b]Department of Bioscience – Microbiology, Aarhus University, Ny Munkegade 116, 8000
9 Aarhus C, Denmark.
10 [c]School of Earth and Environmental Sciences and Centre for Exoplanet Science, University of
11 St Andrews, St Andrews, KY16 9AL Scotland/UK.
12 [d]Department of Geology, University of Tartu, 50411 Tartu, Estonia.
13 [e]Institute of Geology, Karelian Science Centre, Pushkinskaya 11, 185610 Petrozavodsk, Russia.
14 [f]Geological Survey of Norway (NGU), 7491 Trondheim, Norway.
15
16 *Corresponding author: email kart.paiste@ut.ee
17 [1]Present address: Department of Geology, University of Tartu, 50411 Tartu, Estonia.

Abstract

19 The pyrite sulfur isotope record of the 1.98 Ga Zaonega Formation in the Onega Basin, NW

20 Russia, has played a central role in understanding ocean-atmosphere composition and infering

21 worldwide fluctuations of the seawater sulfate reservoir during the pivotal times of the

22 Paleoproterozoic Era. That, in turn, has led to a concept that Earth's atmospheric oxygen levels

23 underwent global-scale changes. Here we present a steady-state isotope mass-balance model to

24 gain insight into the mechanisms governing the sulfur cycle and sulfate reservoir during

25 deposition of the organic-rich Zaonega Formation. We demonstrate that coupling between high

26 microbial sulfate reduction rates and effective sulfate removal by pyrite precipitation can lead

27 to Rayleigh distillation of the basinal sulfate reservoir and development of high amplitude

28 positive $\delta^{34}S$ excursions. This modelling approach illustrates that secular changes in

29 sedimentary pyrite isotope trends can be explained by processes that reflect local (basin-scale)

30 fluctuations in sulfur cycling rather than global mechanisms.

31 **Keywords**: sulfur isotope fractionation, sulfur cycle, mass-balance model, Paleoproterozoic

1. Introduction

33 Biogeochemical sulfur cycling involves a multitude of processes that collectively influence the

34 magnitude of sulfur isotope fractionation between different sulfur species and determine the

35 final sulfur isotope signature captured in the rock record (Farquhar et al., 2010; Fike et al., 2015;

36 Johnston, 2011). Sulfur isotope data have therefore proven useful for paleoenvironmental

37 reconstructions and in obtaining important insight into the evolution of Earth's surface redox

38 environments (Canfield et al., 2010; Habicht et al., 2002; Sim et al., 2011). However, the

39 complex relationships between microbial metabolisms and their immediate environments

40 particularly within dynamic diagenetic settings can have a significant impact on sulfur cycling

41 (Aller et al., 2010; Lin et al., 2016; Paiste et al., 2018). Consequently, disentangling the local

42 from global signals in sulfur isotope records is not straightforward. Ideally, paleo-

43 environmental information is gained from concurrent isotope records of the initial sulfate

44 reservoir and resulting sedimentary sulfide. Complicating this is the fact that sulfate minerals

45 are often not preserved, hence reconstructions of past sulfur cycling commonly rely on sulfide

46 mineral (mainly pyrite) records alone. To address this shortcoming, theoretical models have

47 been used to track processes involved in the production and preservation of sedimentary pyrite

48 (Berner, 1964; Donahue et al., 2008; Habicht et al., 2002; Johnston, 2011; Jørgensen, 1979;

49 Zaback et al., 1993). However, simplifications in models reduce the complex depositional

50 histories of rock successions to a few variables, significantly limiting the sensitivity and

51 resolution of the model predictions when trying to reconstruct biogeochemical sulfur cycling

52 processes.

53 Here we use the 1.98 Ga Zaonega Formation in the Onega Basin of NW Russia (Fig. 1) as a

54 case study to investigate the mechanisms governing the sulfur cycle. The Formation was

55 deposited in a magmatically active basin characterised by high organic carbon content in a

56 mixed siliciclastic-carbonate depositional system that accumulated mostly below wave-base

57 (Črne et al., 2014; Melezhik et al., 2015; Qu et al., 2012). In this study, four sets of drill cores

58 (OPH, FAR-DEEP 12AB, FAR-DEEP 13A, OnZap; Fig. 1, A.1) recover nearly the entire

59 Zaonega Formation as well as the lower part of the overlying Suisari Formation. Our new bulk

60 multiple sulfur isotope (Δ^{33}S, δ^{34}S, Δ^{36}S) and major element data from 185 samples were

61 integrated with previously published data from the OnZap cores (Paiste et al., 2018) to provide

62 a nearly continuous sulfur isotope record of the Zaonega Formation. We show that the pyrite

63 isotope record of the Zaonega Formation can be explained by processes bespoke to local (i.e.

64 basin-scale) depositional settings without the need to invoke worldwide changes in ocean

65 chemistry.

2. Geological context

67 The greenschist facies volcano-sedimentary succession of the Zaonega Formation forms the

68 upper part of the supracrustal succession within the Onega Basin, located on the south-eastern

69 part of the Archean Karelian craton in NW Russia (Melezhik et al., 1999). The Zaonega

70 Formation represents a deep-water shelf-slope-basin setting characterised by syndepositional

71 magmatism and volcanism. Although the exact paleobathymetry is unclear, the predominantly

72 fine-grained textures and dearth of current-generated features imply depths below storm-wave

73 base. The lower part of the Zaonega Formation is typified by organic-rich mudstones. The

74 portion of mudstones decreases upward and dolostone beds become more common, implying a

75 change towards carbonate-dominated depositional system in the upper part of the Formation

76 (Črne et al., 2014). The organic-rich sedimentary rocks are interlayered with mafic lava flows

77 and intersected by mafic intrusions emplaced into unlithified sediments as indicated by their

peperitic contacts. These igneous bodies induced hydrothermal circulation and oil-to-gas cracking of organic-matter in the Formations exceptionally C_{org}-rich sedimentary rocks (Črne et al., 2014; Melezhik et al., 1999; Qu et al., 2012). Following deposition of the Zaonega Formation, the basin was filled by thick sub-aqueously extruded basalts interlayered with rare thin mudstone beds of the Suisari Formation (Krupenik et al., 2011; Melezhik et al., 2015).

Whole-rock and mineral Sm-Nd and Pb-Pb isochrone ages from the Suisari Formation have been used to constrain the minimum depositional age for the Zaonega Formation at 1.98 Ga (Puchtel et al., 1999, 1998). Recent U-Pb zircon dates by Martin et al. (2015) imply that deposition of the Zaonega Formation was between 1982.0 ± 4.5 Ma (tuff in the lower Zaonega Formation) and 1967.6 ± 3.5 Ma (detrital grains in overlying Kondopoga Formation). However, the age constraints of the Zaonega Formation remain a matter of debate (Bekker et al., 2016). Until age relationships are more fully resolved, we adopt 1.98 Ga as the time of accumulation for the Zaonega Formation.

3. Materials and Methods

Samples for bulk pyrite sulfur isotope and major element analyses were taken from three cores in the Onega Basin (Fig. 1): Onega Parametric Hole (OPH, 119 samples), FAR-DEEP 12AB (49 samples) and 13A (17 samples). Data on these samples were combined with published bulk pyrite sulfur isotope and major element data for the OnZap cores (Paiste et al., 2018). A distinctive dolostone marker unit in the upper part of the Zaonega Formation (Črne et al., 2014; Melezhik et al., 2015; Paiste et al., 2018; Qu et al., 2012) is used to correlate the cores. The dolostone is characterised by mm- to 1-cm-thick discontinuous apatite layers at its base (Joosu et al., 2015) and striking black silica veins throughout that can be several meters thick and typically are concident with thin mudstone layers within the dolomite. Detailed descriptions of

4

101   the OPH, FAR-DEEP and OnZap cores are available in Krupenik et al. (2011), Črne et al.

102   (2014) and Paiste et al. (2018), respectively.

103   Major element composition of powdered samples was determined by means of X-ray

104   fluorescence spectrometry (XRF) using a PANalytical Axios at 4 kW. Total sulfur (TS) and

105   total organic carbon (TOC) from decarbonated residues were determined by sealed tube

106   combustion using a Leco SC-444 analyser. Sulfur was extracted from powdered samples by a

107   two-step sequential extraction method modified from Canfield et al. (1986) and isotope

108   composition was measured on a Thermo Finnigan MAT 253 gas source mass spectrometer. The

109   sulfur isotope data are reported using standard delta notation (δ), where: $\delta^{3x}S = 1000 \cdot$

110   ($^{3x}R_{sample}/^{3x}R_{V\text{-}CDT} - 1$), and $^{3x}R = {}^{3x}S/^{32}S$, for $3x = 33$ or 34 and $^{3x}R_{V\text{-}CDT}$ represents the

111   international standard Vienna Canyon Diablo Troilite. We express the minor isotope values

112   using the capital delta notation, $\Delta^{33}S = \delta^{33}S - 1000 \cdot [(1 + \delta^{34}S/1000)^{0.515} - 1]$. Sample

113   reproducibility, as determined by replicate analyses of the in-house standard MSS-1, was

114   generally better than 0.1‰ for $\delta^{34}S$ values, 0.015‰ for $\Delta^{33}S$ and 0.2‰ for $\Delta^{36}S$.

115   The isotope mass-balance model was developed using a steady-state model approach by Zaback

116   et al. (1993) and modified to accommodate the multiple sulfur isotope system. The model

117   comprises three sulfur reservoirs that include seawater sulfate ($SO_4^{2-}{}_{SW}$), pore water sulfate

118   ($SO_4^{2-}{}_{PW}$) and microbially generated sulfide (HS^-) between which sulfur is transported and

119   fractionated (Fig. 3). Model details are given in Supplmentary material.

4. Results

4.1 Stratigraphic multiple sulfur isotope trends in the Zaonega Formation

122   Based on litho- and chemostratigraphic correlations, the studied cores provide a composite,

123   nearly continuous sulfur isotope record of the entire Zaonega Formation and the lower part of

124   the overlying Suisari Formation. The studied stratigraphic record has been subdivided into three

125   Members based on lithological features: Member A is characterised by silicicalstic mudstone

126   (hereafter referred to as mudstone) and dolostone beds alternating with thin graded beds

127   interpreted as turbidites; Member B is marked by exceptionally organic-rich (~5-65 wt.% TOC)

128   mudstone and dolostone deposits (representing the Shunga Event; Kump, 2011); and Member

129   C is represented by impure carbonate and mudstone beds (for more details see Fig. A.1).

130   The lower part of Member A has uniformly negative $\delta^{34}S$ and positive $\Delta^{33}S$ values, followed

131   by an up-section stratigraphic trend towards ^{34}S-enriched sulfides (from $\delta^{34}S$ ~-15‰ to ~+15‰)

132   mirrored by a $\Delta^{33}S$ trend (from ~0.03‰ to ~-0.02‰) (Fig. 2, A.1). This up-section increase in

133   $\delta^{34}S$ and decrease in $\Delta^{33}S$ values continues throughout the lower part of Member B and is

134   accompanied by concomitant increases up to 65 wt.% in TOC and up to 11 wt.% in total sulfur

135   (TS). The upper part of Member B is dominated by sulfides with $\delta^{34}S$ of ~18‰ (18.5 ± 7.7‰,

136   1σ) and $\Delta^{33}S$ of ~-0.03‰ (-0.03‰ ± 0.03, 1σ) but also displays several positive $\delta^{34}S$ excursions

137   reaching values as high as +44‰. Sedimentary pyrites reach their highest $\delta^{34}S$ and lowest $\Delta^{33}S$

138   values in the upper part of Member B whereas the overlying Member C shows an up-section

139   decrease in $\delta^{34}S$ towards ~3‰ and more positive (~0‰) $\Delta^{33}S$ at the top of the section. Thin

140   sedimentary units in Member C occur between thick magmatic packages and are typified by

141   generally low TOC and TS content, the only exception being a ~20 m thick mudstone interval

142   (912–890 m) where TOC is up to 22 wt.%, TS is at 29 wt.% and $\delta^{34}S$ increases to 15‰. The

143   $\Delta^{36}S$ display a pattern similar to and consistent with that of $\delta^{34}S$. The $\Delta^{36}S$ values are ~-0.4‰

144   in Member A, increase to ~0.6‰ in Member B and then turn back to ~-0.1‰ in the upper part

145   of Member C.

4.2 Exploring the sulfur isotope record of the Zaonega Formation

147   In order to test potential mechanisms behind the stratigraphic co-variances observed in the

148   pyrite $\Delta^{33}S$-$\delta^{34}S$-$\Delta^{36}S$ record in the Zaonega Formation, an open-system steady-state isotope

149   mass-balance model (Zaback et al., 1993) was adapted to include the multiple S isotope system

150   (Fig. 3, Supplementary material). The open system assumption was justified by determining the

151   minimum number of pore volumes (n_{min}) of sulfate that was required to account for the

152   measured TS concentrations (Zaback et al., 1993)(Fig. 2). By considering the intrinsic sediment

153   properties (porosity and density) and ambient seawater sulfate (SWS) concentrations, n_{min}

154   compares the amount of sulfur trapped in the sediment as sedimentary sulfide and the amount

155   of sulfur which would have been present as sulfate in the initial porewater. If more sulfide is

156   trapped in the sediment than locked away in the initial porewater (n_{min}>1), then open system

157   conditions prevail, whereas if less sulfate is trapped as sedimentary sulfide than sulfate trapped

158   in the initial porewater (n_{min}<1), then open system conditions are less likely. Further, to explain

159   the unusually positive pyrite $\delta^{34}S$ values in Member B the range and evolution of the basin's

160   sulfate levels were explored by considering potential Rayleigh distillation of the local SWS

161   reservoir (Fig. 3).

162   There is no direct constraint for SWS concentrations during accumulation of the Zaonega

163   Formation, however, a SWS concentration of at least 10 mM was recently estimated for the

164   conformably underlying ~2.0 Ga Tulomozero Formation (Blättler et al., 2018). This suggests

165   n_{min} values >1. On average the n_{min} values are ~7.0 in Member A, ~11.4 in Member B and ~2.2

166   in Member C, which indicate open-system conditions. Lower SWS concentrations (<10 mM)

167   would result in even higher n_{min} values (Fig. 2, Table A.1).

168   The maximum isotope effect between seawater sulfate and microbially reduced sulfur is only

169   expressed when burial of reduced sulfur is very low (fraction of pyrite retained in sediments f_s

170   → 0) and the net isotope fractionation ($^{34}\alpha_0$) approaches that of microbial sulfate reduction

171   ($^{34}\alpha_{MSR}$) (Zaback et al., 1993; see modeling details and sensitivity analysis in Supplementary

172   material). In contrast, if all reduced sulfur formed by MSR is effectively captured as

173   sedimentary pyrite (f_s → 1), $^{34}\alpha_{MSR}$ will only have a small effect on $^{34}\alpha_0$ and the precipitated

174   pyrite will have a similar composition to the initial sulfate. Microbial growth in the subsurface

175   is energy limited and, therefore, sulfate reduction rates in sediments are typically slow (Hoehler

176   and Jørgensen, 2013; Sim et al., 2011; Wing and Halevy, 2014) resulting in large biological

177   fractionations (Aoyama et al., 2014; Pellerin et al., 2015). Based on that, fractionations of

178    $^{34}\alpha_{MSR} = 0.945$, $^{33}\lambda_{MSR} = 0.514$ and $^{36}\lambda_{MSR} = 1.90$, were kept constant throughout the models

179   (for further discussion see Supplementary material, Fig. A.3). Modelled trajectories for sulfide

180   isotopic composition reflect the isotopic evolution of aqueous sulfide that is produced during

181   net sulfate reduction. We assume that the produced aqueous sulfide is rapidly and irreverisibly

182   trapped as sedimentary pyrite (instantaneous product).

183   The lower limit for the starting seawater sulfate isotopic composition was derived from the Ca-

184   sulfate evaporite deposits of the Tulomozero Formation, which record $\delta^{34}S$ of 6‰ and $\Delta^{33}S$ and

185    $\Delta^{36}S$ of ~0‰ (Blättler et al., 2018). For the upper part of the Zaonega Formation, $\delta^{34}S$ of around

186   15‰ and $\Delta^{33}S$ of -0.05‰ has been estimated previously for SWS by Scott et al. (2014) based

187   on the tight clustering of pyrite sulfur isotope data around those values. Following the approach

188   of Scott et al. (2014) the latter estimate can be further refined by including the pyrite sulfur

189   isotope data reported in this study for the upper part of the Zaonega Formation (our Member

190   B). By doing so, the seawater sulfate isotopic composition inferred from pyrite data would have

191   respective $\delta^{34}S$, $\Delta^{33}S$ and $\Delta^{33}S$ values of 17.9 ± 7.8‰ (1S), -0.02 ± 0.03‰ (1S) and 0.04 ±

192   0.23‰ (1S). In the presented models we use $\delta^{34}S_{SWS}$ of 6‰, $\Delta^{33}S_{SWS}$ of -0.01‰ and $\Delta^{36}S_{SWS}$

193   of 0.01‰ values, since these are directly measured from the Tulomozero Formation. However,

194   our data can also be satisfied with values of $\delta^{34}S$ of 18‰, $\Delta^{33}S$ of -0.02‰ and $\Delta^{36}S$ of 0.04‰

195   without significantly changing our interpretation (see model sensitivity analysis in

196   Supplementary material, Fig. A.2).

5. Discussion

5.1 Interpreting the sulfur isotope record of the Zaonega Formation

5.1.1 Preservation of the sulfur isotope record

The organic matter in the Zaonega Formation experienced maturation at temperatures between 350–400 °C during greenschist metamorphism, thus reactions between organic compounds and sulfur-bearing fluids (possibly derived from the Ca-sulfate bearing underlying Tulomozero Formation) could have induced thermochemical sulfate reduction (TSR) and precipitation of late-stage pyrites that carry anomalous isotope signatures deviating from thermodynamic predictions ($\Delta^{33}S$ and $\Delta^{36}S \neq 0$; Amrani, 2014; Ono et al., 2006; Watanabe et al., 2009). However, mass-independent fractionation effects ($\Delta^{36}S/\Delta^{33}S$ slope of ~-1; Ono et al., 2006) typically attributed to TSR (Watanabe et al., 2009) are not evident in the pyrite multiple sulfur isotope data ($\Delta^{36}S/\Delta^{33}S$ slope of ~-5) of the Zaonega Formation (Fig. 4; Paiste et al., 2018).

It is also possible that generation of acid volatile sulfides (AVS) at the expense of pyrite in Members A and B (Asael et al., 2013) was accompanied by isotope exchange between the different sulfide phases. Assuming that the occurrence of ubiquitous late-stage pyrite (e.g. vein pyrite, large pyrite crystals and aggregates; Paiste et al., 2018) reflects multiple stages of (re)crystallisation and/or that the presence of AVS reflects thermal degradation of pyrite (as suggested previously by Asael et al., 2013), several abiogenic mechanisms could have impacted the $\Delta^{33}S$, $\delta^{34}S$, and $\Delta^{36}S$ records, especially in Member B. However, the paired pyrite and AVS $\Delta^{33}S$ and $\delta^{34}S$ data display only small differences of a few ‰ indicating that either pyrite alteration was not accompanied by significant fractionations or the different AVS mineral phases (e.g. pyrrhotite, sphalerite) derived their sulfur from the same reservoir (Paiste et al., 2018). Also, pervasive re-equilibration of both pyrite and AVS appears unlikely because this would have smoothened the stratigraphic variability.

221 Interactions with magmatic intrusions and lava flows can also alter the sulfur isotope

222 composition of the surrounding sedimentary country rocks. Indeed, the pyrite $\Delta^{33}S$-$\delta^{34}S$ profiles

223 of magmatic bodies in Members A and B have the sulfur isotope signature of the country rock

224 at the margins of the bodies and gradually shift, as expected for magmatic sulfur, towards 0‰,

225 at the centres of magmatic bodies where sulfur concentrations are lowest <1 wt.% (Fig. 5).

226 However, this alteration does not extend further into the sediment and is limited to the contact

227 zones with the magmatic bodies. Thus, it is unlikely that magmatic fluids or sulfur leached from

228 the magmatic bodies contributed any significant externally derived sulfur to the sedimentary

229 rocks during diagenesis or metamorphism. The large-scale migrated hydrocarbon interval

230 interpreted as seafloor asphalt spill in FAR-DEEP 12AB (156–136 m; Qu et al., 2012) is

231 isotopically similar to its source rocks in the underlying strata suggesting that magmatically

232 induced migration of hydrocarbons and fluidised sediments did not significantly alter early

233 diagenetic pyrites that were being migrated with them (Fig. 2, Fig. A.1).

234 Although, we cannot conclusively dismiss contributions of pyrite generated by TSR or other

235 late-stage processes, it is unlikely that any of these are the dominant mechanisms for

236 fractionating sulfur isotopes in the Zaonega Formation rocks and the $\Delta^{33}S$, $\delta^{34}S$ and $\Delta^{36}S$ records

237 likely reflect first-order stratigraphic changes in sulfur cycling in the depositional environment.

238 **5.1.2 Member A**

239 In order to reproduce the measured sulfur isotope data for Member A, we constructed a model

240 that produced a set of predictions for sulfide $\Delta^{33}S$-$\delta^{34}S$ ($\Delta^{36}S$-$\delta^{34}S$) pairs that cover a spectrum

241 of isotopic compositions between two opposing endmembers, where one is sulfide produced in

242 open-system MSR ($f_s \rightarrow 0$) and the other being sulfide generated by quantitative reduction (f_s

243 $\rightarrow 1$) of the same initial sulfate. If MSR alone was controlling sulfur isotope fractionations in

244 Member A, the observed pyrite isotope data should converge on the modelled fractionation line.

245   Instead, the measured pyrite $\Delta^{33}S$-$\delta^{34}S$ and $\Delta^{36}S$-$\delta^{34}S$ data fall on a curved mixing line

246   connecting the two sulfide endmembers (Fig. 6.1). Such $\Delta^{33}S$-$\delta^{34}S$-$\Delta^{36}S$ relationship suggests

247   that other processes in addition to MSR (e.g. sedimentary, diagenetic) are contributing to the

248   pyrite sulfur isotope variability.

249   The observed mixing signature can be explained by several processes. For example, it has been

250   proposed that shoaling of anoxic/euxinic deep water could cut off sulfate supply into the

251   sediments and lead to the formation of a separate generation of closed-system pyrite in addition

252   to those that formed previously in open-system conditions (Shen et al., 2011). Under more

253   energetic depositional conditions, episodic sediment reworking could also generate such mixing

254   signatures even under an oxygenated water column by superimposing pyrites that formed at

255   different stages of diagenesis (Aller et al., 2010). Another possibility is that due to fast

256   deposition rates, some pyrite precipitates near the sediment-water interface, where sulfate and

257   iron are not limiting, whereas other pyrite forms later in the burial history from an evolving

258   pore water sulfate pool (Pasquier et al., 2017; Ries et al., 2009).

259   In Member A, n_{min} values well above 1 in both the OPH and FAR-DEEP 12AB data imply an

260   open system but strong correlations between Fe and S in the OPH data suggest high

261   sulfidisation, whereas scattered Fe:S ratios in FAR-DEEP 12AB data suggest a lower degree of

262   sulfidisation (Fig. 7A). Thus, redox conditions were varied across the basin but the sediment

263   was open to sulfate transport. The high n_{min} values (up to 27.9) can be attributed to rapid sulfate

264   consumption within pore waters close to the sediment-water interface or alternatively, to low

265   sedimentation rates in order to sustain prolonged connectivity between pore space and the

266   overlying water column. However, the latter seems unlikely for Member A, as the occurrence

267   of coarser-grained sediment-gravity flow and turbidity-current deposits in the lower part of the

268   FAR-DEEP 12AB core argue for relatively rapid deposition. Although the correlative intervals

269   between OPH and FAR-DEEP 12AB cores have ~8‰ difference in $\delta^{34}S$ values, ~-11‰ versus

270 ~-19‰, respectively, this is explained readily by facies changes: OPH is characterized by

271 mudstones and calcareous mudstones whereas FAR-DEEP 12AB is coarser-grained facies and

272 these would have higher permeability and thus favour more open-system conditions as well as

273 lower sulfidisation relative to the finer-grained OPH section.

274 While it is difficult to confidently determine from bulk samples if changes in sedimentation,

275 diagenesis or both are responsible for the mixing of pyrites in Member A, it is likely that

276 depositional style played an important role in the final S isotope composition of the sedimentary

277 pyrites of the Zaonega Formation. In any case, the stratigraphically increasing δ^{34}S and Δ^{36}S

278 and decreasing Δ^{33}S trends infer a transition to lower connectivity between the SWS pool and

279 sedimentary pore waters.

5.1.3 Member B

281 In the upper part of Member A and throughout Member B, pyrites with more positive $\delta^{34}S_{pyr}$

282 and Δ^{36}S and negative Δ^{33}S than the initial SWS ($\delta^{34}S_{SWS}$ of 6‰, $\Delta^{33}S_{SWS}$ of -0.01‰, and

283 $\Delta^{36}S_{SWS}$ of 0.01‰) can be explained by an evolving basinal sulfate pool as a result of increased

284 pyrite burial (Fig. 3). The organic carbon content of >5 wt.% in the sedimentary rocks of the

285 Zaonega Formation is significantly higher than is typical for marine sediments that accumulated

286 under oxidizing conditions throughout the Phanerozoic (Lyons and Severmann, 2006). Such

287 high organic carbon loading could support a large population of sulfate reducers within the

288 sediment and increase the demand for sulfate (Habicht and Canfield, 1997). Accordingly, the

289 consumption of sulfate via MSR could exceed its replenishment from the overlying water

290 column and foster sulfate limitation in pore waters (Goldhaber and Kaplan, 1975; Jørgensen,

291 1979). This would result in small net fractionation, if the reduced sulfur was scavenged by

292 reactive iron and effectively converted into pyrite. This is in agreement with the strong

293 correlation of Fe:S ratios in Member B and n_{min} >>1 that suggest intense sulfate diffusion into

294   pore water, possibly at a very shallow redoxcline where sulfate and iron would have been

295   readily available (Fig. 7).

296   Complicating the already complex depositional environment of the organic-rich Zaonega rocks,

297   the episodic magmatic and volcanic activity would have influenced the configuration and

298   connectivity of the basin and regulated nutrient fluxes to promote primary production (Fig. 3).

299   Lithological evidence suggests a shift towards predominantly carbonate precipitation in the

300   upper part of the Zaonega Formation implying changes in the depositional conditions and

301   possibly basin shallowing (Melezhik et al., 2015; Paiste et al., 2018). Hence, it is entirely

302   feasible that semi-restriction or occasional closure of the Onega Basin occurred during

303   deposition of the upper part of the Zaonega Formation.

304   Melezhik et al. (1999) have applied the TS/TOC paleosalinity proxy to suggest that the

305   predominantly low TS/TOC ratios (<0.36) combined with elevated TS and TOC concentrations,

306   and a positive correlation between the two parameters in the Zaonega Formation succession, is

307   representative of sediment deposition in a swampy brackish water lagoon under non-euxinic

308   conditions. Indeed, using the refined baseline values for the TS/TOC proxy from Wei and Algeo

309   (2019) the <0.1 TS/TOC ratios determined for Member A are indicative of a freshwater

310   environment, whereas varying freshwater to brackish and/or marine conditions characterize

311   Member B (TS/TOC mostly between 0.1 and 0.5) and marine conditions typify Member C

312   (TS/TOC >0.5) (Fig. 8). If taken at face value, the highly variable TS/TOC ratios in Member B

313   could be attributed to a semi-restricted basin. However, we are cautious about using the

314   TS/TOC proxy too liberally in any interpretations because, firstly, it has been calibrated for

315   modern sediments and it is not clear how well it applies to metasedimentary rocks and,

316   secondly, the Zaonega sediments were subject to much magmatic or hydrothermal activity and

317   associated hydrocarbon generation and seepage. We do note, though, that the relatively high

318   TS/TOC ratios in Member B imply that MSR was not sulfate-limited. In a semi-restricted

setting, the consumption of sulfate by MSR and increased pyrite retention in sediments would cause distillation of the basinal sulfate reservoir and generate parallel increases in $\delta^{34}S_{SWS}$ and $\delta^{34}S_{pyr}$ exhibiting Rayleigh behaviour of ^{33}S, ^{34}S and ^{36}S as the residual sulfate becomes enriched in ^{34}S (Fike et al., 2015; Fike and Grotzinger, 2010; Gomes and Hurtgen, 2013).

Assuming that a constant flux of sulfate entered the pore waters, whereas only a small fraction of the sulfur was returned into the water column (1 - f_s), basinal sulfate levels would have decreased gradually. According to the model for Member A, retention of half of the sulfate that entered the sediments ($f_s = 0.5$) would correspond to a net fractionation of 0.974 for $^{34}\alpha_0$ paired with $^{33}\lambda_0$ of 0.510 and $^{36}\lambda_0$ of 1.926. If we use these parameters to model the Rayleigh distillation of the sulfate reservoir, the trajectory in which the basinal sulfate isotopic composition ($\Delta^{33}S_{SWS}$, $\delta^{34}S_{SWS}$ and $\Delta^{36}S_{SWS}$) evolves is controlled by the overall isotope effect of the sedimentary system. Previous work assumed that at sulfate concentrations <200 μM (Habicht et al., 2002) microbial fractionation becomes suppressed; however, in natural environments low respiration rates can lead to large fractionations even under extremely low sulfate levels (<10 μM) (Crowe et al., 2014; Gomes and Hurtgen, 2013; Wing and Halevy, 2014). Thus, by using the same input parameters as in Member A, the model generates a set of predictions for sedimentary pyrites in Member B that formed after a fraction of the initial sulfate was removed from the system (f_{SWS}; Fig. 6.2).

By decreasing the size of the sulfate reservoir by 80% ($f_{SWS} = 0.2$), due to the basinal sulfate being reduced and buried as pyrite, our model reproduces the most extreme $\delta^{34}S$ values of 44‰, $\Delta^{33}S$ of -0.06‰ and $\Delta^{36}S$ of 0.6‰ found in the upper strata of Member B. There, where rapid sulfate turnover is expected due to abundant organic matter (TOC up to 45 wt.%), the sediments display relatively constant f_s values (0.8–0.96), which is consistent with an increased sink for sulfide. Further, the positive sulfur isotope excursions where $\delta^{34}S$ evolves towards highly

343   positive values (>+30‰) occur over a few meters of strata. In the modern oceans with sulfate

344   concentrations of 28 mM a multi-million-year residence time (>8 Myr) is estimated for marine

345   sulfate (Berner, 2001; Canfield, 2004). Thus, even if the SWS reservoir during the Zaonega

346   time was a fraction of the modern, it is unlikely that the punctuated $\Delta^{33}S$-$\delta^{34}S$ ($\Delta^{36}S$) excursions

347   reflect global perturbations in the sulfur cycle, as it would require a mechanism capable of

348   catalysing repeated expansions and contractions in the sulfate reservoir over a relatively short

349   time (<<million years). However, such high frequency fluctuations in the size of the sulfate

350   reservoir are consistent with a semi-restricted basin (e.g. the Baltic Sea; Döös et al., 2004), as

351   sluggish water circulation could periodically cut off sulfate supply or rapid sulfate consumption

352   could lower basinal sulfate concentrations faster than it was replenished (Fig. 3).

353   In the upper part of Member B (1130–1080 m interval) there are, though, a significant number

354   of $\Delta^{33}S$ values more negative and $\Delta^{36}S$ more positive than predicted by the modelled pyrite

355   field. These values cannot be reproduced even by accommodating almost the full range of

356   fractionations associated with MSR ($^{34}\alpha_{MSR}$ 0.93–0.98; Aoyama et al., 2014; Johnston, 2011;

357   Sim et al., 2011). The measured $\Delta^{33}S$-$\delta^{34}S$ pairs that deviate from model predictions occur in

358   the 1130–1080 m interval where the concomitant up-section decrease in TOC and TS and a

359   wider span of f_s values (~0.6–0.96) suggest lower degrees of sulfate reduction and/or more

360   open-system conditions. Generally low sulfate reduction rates and open-system conditions lead

361   to large net fractionations between sulfate and sulfide but the highly positive $\delta^{34}S$, $\Delta^{36}S$ and

362   negative $\Delta^{33}S$ values within this interval are at odds with this assumption. However, the

363   description of several generations of pyrites within the OnZap section by Paiste et al. (2018)

364   imply that the occurrence of genetically distinct pyrites could account for the anomalous bulk

365   pyrite S-isotope signatures in the 1130–1080 m interval. Most of these anomalous samples are

366   from carbonate beds where multiple generations of pyrite co-occur, including large (>100 μm)

367   disseminated euhedral to anhedral pyrite crystals, irregular aggregates of inclusion-rich pyrite

368   and fine-grained (~10 μm) euhedral and typically octahedral pyrite. The large pyrite likely

369   precipitated from evolved pore waters during late-stage diagenesis whereas the fine-grained

370   pyrites are early-diagenetic precipitates. As in Member A, this can be tested by mixing of two

371   sulfide endmembers, where one formed in open- and the other in closed-system conditions.

372   Using this framework, our model satisfies more than 95% of the measured pyrite sulfur isotope

373   compositions (Fig. 6.2).

5.1.4 Member C

375   In Member C the measured pyrite compositions can be explained by a general transition towards

376   more open-system conditions, as indicated by the up-section shift in f_s values from around 0.9

377   to 0.6 (Fig. 6.3). Furthermore, reduced organic carbon load and lower rates of MSR would allow

378   for a longer residence time of sulfate and subsequently diminish the Rayleigh effect on the

379   basinal reservoir. Such a scenario is supported by n_{min} values that generally decrease in the

380   upper part of Members B and C and are typically associated with lower TOC concentrations,

381   which is consistent with lower rates of sulfate reduction (Fig.2, 7B). These trends agree with

382   the wide spread of Fe:S ratios indicating a low degree of sulfidisation (Fig. 7A). The occurrence

383   of a mudstone interval in Member C (912–890 m) with very high TOC (up to 22 wt.%) and TS

384   (up to 29 wt.%) concentrations and strong Fe:S correlation imples episodes of more rapid

385   sulfate consumption and increased pyrite burial. This interval is sandwiched between thick

386   packages of mafic lava flows and displays extremely high n_{min} values, likely due to locally high

387   geothermal gradients that induced hydrothermal fluid circulation and rapid sulfate consumption

388   within pore waters. This is also in agreement with our model predictions, as in the 912–890 m

389   interval the measured pyrite $\Delta^{33}S$-$\delta^{34}S$ data converge on the modelled fractionation line where

390   f_s values are close to 1 and the pyrite isotopic composition approaches that of the initial sulfate.

391   However, these effects would be short lived and not persisting long enough to affect the basinal

392   sulfate pool. Another possibility to explain the very high TS concentrations is generation of

393 secondary pyrite via reactions between sulfur-bearing magmatic fluids and iron in sediments.

394 As documented above, addition of magmatic sulfur cannot be fully excluded but is unlikely

395 since the studied magmatic bodies incorporate sulfur from the adjacent sediments rather than

396 add magmatic sulfur to the diagenetic environment.

5.1.5 Implications for the global seawater sulfate reservoir

398 The main result of our modelling efforts is that in order to precipitate the abundant pyrite,

399 explain the n_{min} values >>1 and short-lived high amplitude $\delta^{34}S$ (>30‰) excursions, a sizeable

400 basinal sulfate reservoir had to be maintained during deposition of the Zaonega Formation. We

401 enviage that basinal sulfate levels were replenished via episodic inflow from an oceanic

402 reservoir. In effect, the $\delta^{34}S_{SWS}$ of 6‰, $\Delta^{33}S_{SWS}$ of -0.01‰ and $\Delta^{36}S_{SWS}$ of 0.01‰ (Blättler et

403 al., 2018) used in our model could represent the lower limit for the sulfate composition of the

404 global ocean during the Zaonega time. An upper estimate inferred in a similar way as in Scott

405 et al. (2014) from pyrite sulfur isotope data suggests $\delta^{34}S_{SWS}$ of 18‰, $\Delta^{33}S_{SWS}$ of -0.02‰ and

406 $\Delta^{36}S_{SWS}$ of 0.04‰ during deposition of the upper Zaonega Formation (Member B). However,

407 closure of the basin likely commenced (Melezhik et al., 2015) during deposition of the upper

408 part of the Zaonega Formation and may have restricted water circulation with the ocean. Thus,

409 even if pyrites in Member B capture the initial sulfate signal, it is not clear if it represents the

410 oceanic or basinal sulfate pool. Nevertheless, the respective range of $\delta^{34}S_{SWS}$, $\Delta^{33}S_{SWS}$ and

411 $\Delta^{36}S_{SWS}$ values between 6–18‰, -0.01–-0.02‰ and 0.01–0.04‰ are in agreement with those

412 reported in Crockford et al. (2019) for the time period between 2.0–1.9 Ga. However, the

413 suggested range of $\delta^{34}S_{SWS}$, $\Delta^{33}S_{SWS}$ and $\Delta^{36}S_{SWS}$ values are an indirect consequence of our

414 modelling exercise and need further evaluation. Combining all of the above, the most

415 circumspect use of the pyrite sulfur isotope data of the Zaonega Formation is to first understand

416 the nature of the basinal sulfur cycle before considering those data as a proxy to estimate large-

417 scale perturbations in the global SWS reservoir. We also note that isotope signatures ascribed

418 to biological and abiogenic processes could be difficult to distinguish in bulk samples and

419 deeper insight on AVS formation and abiogenic reactions between sulfur-bearing fluids and

420 organic matter could be obtained via petrographically constrained micro-scale analyses (e.g.

421 SIMS investigation) of different sulfide minerals and pyrite generations.

Conclusions

423 The pyrite multiple sulfur isotope record of the Paleoproterozoic Zaonega Formation can be

424 reproduced with a steady-state isotope mass-balance model by including an evolving basinal

425 sulfate reservoir affected by Rayleigh distillation. While the rate of sulfate reduction versus

426 transport largely controls sedimentary sulfur cycling in marine sediments, in a restricted basin

427 the increased removal of sulfate by pyrite precipitation and/or changes in basin connectivity

428 can generate secular changes in the quantity and composition of basinal sulfate. Given that the

429 Zaonega Formation was deposited in a magmatically active and dynamic depositional setting,

430 the entire pyrite isotope record and the mass dependent $\Delta^{33}S$-$\delta^{34}S$-$\Delta^{36}S$ relationships can be

431 explained by variations in local sedimentological and biogeochemical conditions without the

432 need for invoking global changes in ocean chemistry. This becomes even more obvious when

433 realising that positive sulfur isotope excursions with high amplitude $\delta^{34}S$ values occur over only

434 a few meters of strata in the Zaonega Formation, which would require repeated expansions and

435 contractions in the seawater sulfate reservoir over unreasonably short time spans (i.e. likely

436 much less than a million years). Our modelling exercise, albeit not capable of constraining

437 unequivocally SWS concentrations at ~1.98 Ga, does demonstrate that a substantial sulfate

438 reservoir was required in order to account for the abundant pyrite in the Zaonega Formation.

Acknowledgements

References

Aller, R.C., Madrid, V., Chistoserdov, A., Aller, J.Y., Heilbrun, C., 2010. Unsteady diagenetic processes and sulfur biogeochemistry in tropical deltaic muds: Implications for oceanic isotope cycles and the sedimentary record. Geochimica et Cosmochimica Acta 74, 4671–4692. https://doi.org/10.1016/j.gca.2010.05.008

Amrani, A., 2014. Organosulfur Compounds: Molecular and Isotopic Evolution from Biota to Oil and Gas. Annu Rev Earth Pl Sc 42, 733–768. https://doi.org/10.1146/annurev-earth-050212-124126

Aoyama, S., Nishizawa, M., Takai, K., Ueno, Y., 2014. Microbial sulfate reduction within the Iheya North subseafloor hydrothermal system constrained by quadruple sulfur isotopes. Earth Planet Sc Lett 398, 113–126. https://doi.org/10.1016/j.epsl.2014.04.039

Asael, D., Tissot, F.L.H., Reinhard, C.T., Rouxel, O., Dauphas, N., Lyons, T.W., Ponzevera, E., Liorzou, C., Cheron, S., 2013. Coupled molybdenum, iron and uranium stable isotopes as oceanic paleoredox proxies during the Paleoproterozoic Shunga Event. Chemical Geology 362, 193–210. https://doi.org/10.1016/j.chemgeo.2013.08.003

Bekker, A., Krapež, B., Müller, S.G., Karhu, J.A., 2016. A short-term, post-Lomagundi positive C isotope excursion at *c.* 2.03 Ga recorded by the Wooly Dolomite, Western Australia. Journal of the Geological Society 173, 689–700. https://doi.org/10.1144/jgs2015-152

Berner, R.A., 2001. Modeling atmospheric O 2 over Phanerozoic time.

Berner, R.A., 1964. An idealized model of dissolved sulfate distribution in recent sediments. Geochimica et Cosmochimica Acta 28, 1497–1503.

Berner, R.A., Raiswell, R., 1983. Burial of organic carbon and pyrite sulfur in sediments over phanerozoic time: a new theory. Geochimica et Cosmochimica Acta 47, 855–862. https://doi.org/10.1016/0016-7037(83)90151-5

Blättler, C.L., Claire, M.W., Prave, A.R., Kirsimäe, K., Higgins, J.A., Medvedev, P.V., Romashkin, A.E., Rychanchik, D.V., Zerkle, A.L., Paiste, K., Kreitsmann, T., Millar, I.L., Hayles, J.A., Bao, H., Turchyn, A.V., Warke, M.R., Lepland, A., 2018. Two-billion-year-old evaporites capture Earth's great oxidation. Science eaar2687. https://doi.org/10.1126/science.aar2687

Canfield, D.E., 2004. The evolution of the Earth surface sulfur reservoir. Am J Sci 304, 839–861. https://doi.org/10.2475/ajs.304.10.839

Canfield, D.E., Farquhar, J., Zerkle, A.L., 2010. High isotope fractionations during sulfate reduction in a low-sulfate euxinic ocean analog. Geology 38, 415–418. https://doi.org/10.1130/G30723.1

Canfield, D.E., Raiswell, R., Westrich, J.T., Reaves, C.M., Berner, R.A., 1986. The use of chromium reduction in the analysis of reduced inorganic sulfur in sediments and shales. Chemical Geology 54, 149–155. https://doi.org/10.1016/0009-2541(86)90078-1

Črne, A.E., Melezhik, V.A., Lepland, A., Fallick, A.E., Prave, A.R., Brasier, A.T., 2014. Petrography and geochemistry of carbonate rocks of the Paleoproterozoic Zaonega Formation, Russia: Documentation of C-13-depleted non-primary calcite. Precambrian Res 240, 79–93. https://doi.org/DOI 10.1016/j.precamres.2013.10.005

Crockford, P.W., Kunzmann, M., Bekker, A., Hayles, J., Bao, H., Halverson, G.P., Peng, Y., Bui, T.H., Cox, G.M., Gibson, T.M., Wörndle, S., Rainbird, R., Lepland, A., Swanson-Hysell, N.L., Master, S., Sreenivas, B., Kuznetsov, A., Krupenik, V., Wing, B.A., 2019. Claypool continued: Extending the isotopic record of sedimentary sulfate. Chemical Geology. https://doi.org/10.1016/j.chemgeo.2019.02.030

Crowe, S.A., Paris, G., Katsev, S., Jones, C., Kim, S.-T., Zerkle, A.L., Nomosatryo, S., Fowle, D.A., Adkins, J.F., Sessions, A.L., Farquhar, J., Canfield, D.E., 2014. Sulfate was a trace constituent of Archean seawater. Science 346, 735–739. https://doi.org/10.1126/science.1258966

Donahue, M.A., Werne, J.P., Meile, C., Lyons, T.W., 2008. Modeling sulfur isotope fractionation and differential diffusion during sulfate reduction in sediments of the Cariaco Basin. Geochimica et Cosmochimica Acta 72, 2287–2297. https://doi.org/10.1016/j.gca.2008.02.020

Döös, K., Meier, H.E.M., Döscher, R., 2004. The Baltic Haline Conveyor Belt or The Overturning Circulation and Mixing in the Baltic. AMBIO: A Journal of the Human Environment 33, 261–266. https://doi.org/10.1579/0044-7447-33.4.261

Farquhar, J., Wu, N., Canfield, D.E., Oduro, H., 2010. Connections between Sulfur Cycle Evolution, Sulfur Isotopes, Sediments, and Base Metal Sulfide Deposits. Economic Geology 105, 509–533. https://doi.org/10.2113/gsecongeo.105.3.509

Fike, D.A., Bradley, A.S., Rose, C.V., 2015. Rethinking the Ancient Sulfur Cycle. Annu Rev Earth Pl Sc 43, 593–622. https://doi.org/10.1146/annurev-earth-060313-054802

Fike, D.A., Grotzinger, J.P., 2010. A $\delta^{34}SSO_4$ approach to reconstructing biogenic pyrite burial in carbonate-evaporite basins: An example from the Ara Group, Sultanate of Oman. Geology 38, 371–374. https://doi.org/10.1130/G30230.1

Goldhaber, M.B., Kaplan, I.R., 1975. Controls and consequences of sulfate reduction rates in recent marine sediments. Soil Science 119.

Gomes, M.L., Hurtgen, M.T., 2013. Sulfur isotope systematics of a euxinic, low-sulfate lake: Evaluating the importance of the reservoir effect in modern and ancient oceans. Geology 41, 663–666. https://doi.org/10.1130/G34187.1

Habicht, K.S., Canfield, D.E., 1997. Sulfur isotope fractionation during bacterial sulfate reduction in organic-rich sediments. Geochimica et Cosmochimica Acta 61, 5351–5361. https://doi.org/10.1016/S0016-7037(97)00311-6

Habicht, K.S., Gade, M., Thamdrup, B., Berg, P., Canfield, D.E., 2002. Calibration of sulfate levels in the Archean Ocean. Science 298, 2372–2374. https://doi.org/DOI 10.1126/science.1078265

Hoehler, T.M., Jørgensen, B.B., 2013. Microbial life under extreme energy limitation. Nature Reviews Microbiology 11, 83–94. https://doi.org/10.1038/nrmicro2939

Johnston, D.T., 2011. Multiple sulfur isotopes and the evolution of Earth's surface sulfur cycle. Earth-Sci Rev 106, 161–183. https://doi.org/DOI 10.1016/j.earscirev.2011.02.003

Joosu, L., Lepland, A., Kirsimae, K., Romashkin, A.E., Roberts, N.W., Martin, A.P., Crne, A.E., 2015. The REE-composition and petrography of apatite in 2 Ga Zaonega Formation, Russia: The environmental setting for phosphogenesis. Chemical Geology 395, 88–107. https://doi.org/10.1016/j.chemgeo.2014.11.013

Jørgensen, B.B., 1979. A theoretical model of the stable sulfur isotope distribution in marine sediments. Geochimica et Cosmochimica Acta 43, 363–374. https://doi.org/10.1016/0016-7037(79)90201-1

Krupenik, V.A., Akhmedov, A.M., Sveshnikova, K.Y., 2011. Isotopic composition of carbon, oxygen and sulfur in the Ludicovian and Jatulian rocks, in: Glushanin, L.V., Sharov, N.V., Shchiptsov, V.V. (Eds.), The Onega Paleoproterozoic Structure (Geology, Tectonics, Deep Structure, Minerogeny). Institute of Geology, Karelian Research Centre RAS, Petrozavodsk, pp. 250–255.

Kump, L.R., 2011. Isotopic Evidence for Massive Oxidation of Organic Matter Following the Great Oxidation Event. Science 334, 1694–1696. https://doi.org/10.1126/science.1213999

Lin, Z., Sun, X., Peckmann, J., Lu, Y., Xu, L., Strauss, H., Zhou, H., Gong, J., Lu, H., Teichert, B.M.A., 2016. How sulfate-driven anaerobic oxidation of methane affects the sulfur isotopic composition of pyrite: A SIMS study from the South China Sea. Chemical Geology 440, 26–41. https://doi.org/10.1016/j.chemgeo.2016.07.007

Lyons, T.W., Severmann, S., 2006. A critical look at iron paleoredox proxies: New insights from modern euxinic marine basins. Geochimica et Cosmochimica Acta 70, 5698–5722. https://doi.org/10.1016/j.gca.2006.08.021

Martin, A.P., Prave, A.R., Condon, D.J., Lepland, A., Fallick, A.E., Romashkin, A.E., Medvedev, P.V., Rychanchik, D.V., 2015. Multiple Palaeoproterozoic carbon burial episodes and excursions. Earth Planet Sc Lett 424, 226–236. https://doi.org/10.1016/j.epsl.2015.05.023

Melezhik, V.A., Fallick, A.E., Brasier, A.T., Lepland, A., 2015. Carbonate deposition in the Palaeoproterozoic Onega basin from Fennoscandia: a spotlight on the transition from the Lomagundi-Jatuli to Shunga events. Earth-Sci Rev 147, 65–98. https://doi.org/10.1016/j.earscirev.2015.05.005

Melezhik, V.A., Fallick, A.E., Filippov, M.M., Larsen, O., 1999. Karelian shungite—an indication of 2.0-Ga-old metamorphosed oil-shale and generation of petroleum: geology, lithology and geochemistry. Earth-Science Reviews 47, 1–40. https://doi.org/10.1016/S0012-8252(99)00027-6

Ono, S., Wing, B., Johnston, D., Farquhar, J., Rumble, D., 2006. Mass-dependent fractionation of quadruple stable sulfur isotope system as a new tracer of sulfur biogeochemical cycles. Geochimica et Cosmochimica Acta 70, 2238–2252. https://doi.org/DOI 10.1016/j.gca.2006.01.022

Paiste, K., Lepland, A., Zerkle, A.L., Kirsimäe, K., Izon, G., Patel, N.K., McLean, F., Kreitsmann, T., Mänd, K., Bui, T.H., Romashkin, A.E., Rychanchik, D.V., Prave, A.R., 2018. Multiple sulphur isotope records tracking basinal and global processes in the 1.98 Ga Zaonega Formation, NW Russia. Chemical Geology 499, 151–164. https://doi.org/10.1016/j.chemgeo.2018.09.025

Pasquier, V., Sansjofre, P., Rabineau, M., Revillon, S., Houghton, J., Fike, D.A., 2017. Pyrite sulfur isotopes reveal glacial−interglacial environmental changes. Proceedings of the National Academy of Sciences 114, 5941–5945. https://doi.org/10.1073/pnas.1618245114

578 Pellerin, A., Bui, T.H., Rough, M., Mucci, A., Canfield, D.E., Wing, B.A., 2015. Mass-
579   dependent sulfur isotope fractionation during reoxidative sulfur cycling: A case study
580   from Mangrove Lake, Bermuda. Geochimica et Cosmochimica Acta 149, 152–164.
581   https://doi.org/10.1016/j.gca.2014.11.007

582 Puchtel, I.S., Arndt, N.T., Hofmann, A.W., Haase, K.M., Kroner, A., Kulikov, V.S., Kulikova,
583   V.V., Garbe-Schonberg, C.D., Nemchin, A.A., 1998. Petrology of mafic lavas within
584   the Onega plateau, central Karelia: evidence for 2.0 Ga plume-related continental crustal
585   growth in the Baltic Shield. Contributions to Mineralogy and Petrology 130, 134–153.
586   https://doi.org/10.1007/s004100050355

587 Puchtel, I.S., Brugmann, G.E., Hofmann, A.W., 1999. Precise Re-Os mineral isochron and Pb-
588   Nd-Os isotope systematics of a mafic-ultramafic sill in the 2.0 Ga Onega plateau (Baltic
589   Shield). Earth Planet Sc Lett 170, 447–461. https://doi.org/10.1016/s0012-
590   821x(99)00118-1

591 Qu, Y., Crne, A.E., Lepland, A., Van Zuilen, M.A., 2012. Methanotrophy in a Paleoproterozoic
592   oil field ecosystem, Zaonega Formation, Karelia, Russia. Geobiology 10, 467–478.
593   https://doi.org/Doi 10.1111/Gbi.12007

594 Ries, J.B., Fike, D.A., Pratt, L.M., Lyons, T.W., Grotzinger, J.P., 2009. Superheavy pyrite (
595   34Spyr > 34SCAS) in the terminal Proterozoic Nama Group, southern Namibia: A
596   consequence of low seawater sulfate at the dawn of animal life. Geology 37, 743–746.
597   https://doi.org/10.1130/G25775A.1

598 Scott, C., Wing, B.A., Bekker, A., Planavsky, N.J., Medvedev, P., Bates, S.M., Yun, M., Lyons,
599   T.W., 2014. Pyrite multiple-sulfur isotope evidence for rapid expansion and contraction
600   of the early Paleoproterozoic seawater sulfate reservoir. Earth Planet Sc Lett 389, 95–
601   104. https://doi.org/DOI 10.1016/j.epsl.2013.12.010

602 Shen, Y., Farquhar, J., Zhang, H., Masterson, A., Zhang, T., Wing, B.A., 2011. Multiple S-
603   isotopic evidence for episodic shoaling of anoxic water during Late Permian mass
604   extinction. Nature Communications 2. https://doi.org/10.1038/ncomms1217

605 Sim, M.S., Bosak, T., Ono, S., 2011. Large Sulfur Isotope Fractionation Does Not Require
606   Disproportionation. Science 333, 74–77. https://doi.org/10.1126/science.1205103

607 Watanabe, Y., Farquhar, J., Ohmoto, H., 2009. Anomalous fractionations of sulfur isotopes
608   during thermochemical sulfate reduction. Science 324, 370–373.
609   https://doi.org/10.1126/science.1169289

610 Wei, W., Algeo, T.J., 2019. Elemental proxies for paleosalinity analysis of ancient shales and
611   mudrocks. Geochimica et Cosmochimica Acta.
612   https://doi.org/10.1016/j.gca.2019.06.034

613 Wing, B.A., Halevy, I., 2014. Intracellular metabolite levels shape sulfur isotope fractionation
614   during microbial sulfate respiration. Proceedings of the National Academy of Sciences
615   111, 18116–18125. https://doi.org/10.1073/pnas.1407502111

616 Zaback, D.A., Pratt, L.M., Hayes, J.M., 1993. Transport and reduction of sulfate and
617   immobilization of sulfide in marine black shales. Geology 21, 141–144.
618   https://doi.org/10.1130/0091-7613(1993)021<0141:TAROSA>2.3.CO;2

Figure captions

Figure 1. Simplified geological map of the Onega Basin in Karelia, Russia and positions of

drill cores (white circles). Inset map shows the distribution of Paleoproterozoic rocks (black) in

Fennoscandia and the location of the Onega Basin (black square).

623 **Figure 2.** Composite stratigraphic $\delta^{34}S$ and $\Delta^{33}S$, TS, TOC and calculated n_{min} profiles for the

624 Onega Parametric Hole (OPH), FAR-DEEP (FD) and OnZap (OZ) cores from the Zaonega and

625 lower part of the Suisari Formations. The succession has been subdivided into three Members

626 (A–C; for more details see Supplementary materials). Black and grey bars on core profiles show

627 positions of sedimentary and magmatic intervals, respectively. Black (from sedimentary rocks)

628 and grey (from magmatic rocks) dots represent data from this study, blue dots from Paiste et al.

629 (2018) and yellow dots from Melezhik et al. (2012, 2015). The n_{min} values were calculated at

630 28 mM (crimson dots), 10 mM (pink dots) and 2 mM (green dots) seawater sulfate

631 concentrations $[SO_4^{2-}]$. Green arrows represent data points that fall outside of the plotted range

632 of n_{min} values.

633 **Figure 3.** Interpreted semirestricted depositional setting of the Zaonega Formation and inferred

634 sulfur metabolisms including microbial sulfate reduction (A) and sulfide oxidation (B). White

635 arrows illustrate sulfur cycling within the basin and the pathways involved in transport and

636 isotopic fractionation of sulfur in the diagenetic environment. Organic matter (OM) is delivered

637 into sediments via sinking particles of CO_2-fixing autotrophic biomass as well as via

638 hydrocarbon seepage and methanotrophy. The steady-state S isotope mass-balance model

639 (modified after Zaback et al., 1993) used to calculate the model fields in Fig. 6 is illustrated on

640 the right; the boxes represent sulfur reservoirs (SW = seawater, PW = pore water and Py =

641 pyrite) and white arrows indicate fluxes of sulfur ($\phi_i\delta^{3x}S_i$) along different pathways, as

642 described in the supplementary material.

643 **Figure 4.** A compilation of pyrite quadruple sulfur isotope data from the Zaonega and Suisari

644 Formations. Grey circles represent Member A, black circles Member B and blue circles

645 Member C. Dashed line represents an estimated slope of -5.14 for measured pyrite $\Delta^{33}S$-$\delta^{34}S$-

646 $\Delta^{36}S$ data (R^2=0.54).

647 **Figure 5.** A. Triple isotope plot of sulfide isotope data from magmatic bodies in the Zaonega

648 Formation. Coloured dots represent paired $\Delta^{33}S$-$\delta^{34}S$ data from different magmatic bodies in

649 the FAR-DEEP 12AB (FD12AB) and FAR-DEEP 13A (FD13A) cores. B. An example of $\delta^{34}S$

650 (left) and $\Delta^{33}S$ (right) profile through a gabbro in FAR-DEEP 12AB, depth 484–414 m.

651 Numbers and black arrows denote locations of core pictures used to illustrate the gabbro within

652 the contact zones and centres.

653 **Figure 6.** Measured and modelled pyrite $\delta^{34}S$ and $\Delta^{33}S$ data for 1) Member A; 2) Member B;

654 3) Member C and 4) all data. Grey curved lines display vectors for modelled pyrite $\Delta^{33}S$-$\delta^{34}S$

655 pairs that formed from sulfate with an isotope composition at the right end of the curve, yellow

656 dotted curved lines represent mixing between two sulfide endmembers and black arrows the

657 trajectory for sulfate isotope composition according to Rayleigh fractionation of the initial

658 seawater sulfate (orange square) with $\delta^{34}S=6‰$ and $\Delta^{33}S=0‰$ (taken from Blättler et al., 2018).

659 **Figure 7.** A. Measured total sulfur (TS) and iron (TFe) concentrations. B. Calculated n_{min}

660 plotted against total organic carbon (TOC) concentrations from Leco analyses. Blue circles

661 represent Member A, black circles Member B and grey circles Member C.

662 **Figure 8.** Measured total sulfur (TS) versus total organic carbon (TOC) concentrations from

663 siliciclastic mudstones. Data has been filtered according to Wei and Algeo (2019) to include

664 only samples that contain >1 wt.% TOC and lack significant carbonate component. The normal

665 marine trend (0.36) of Berner and Raiswell (1983) is shown as a black dotted line and black

666 solid lines represent threshold values determined for freshwater (<0.1) and marine (>0.5)

667 environments from Wei and Algeo (2019). Blue, black and grey circles represent Member A,

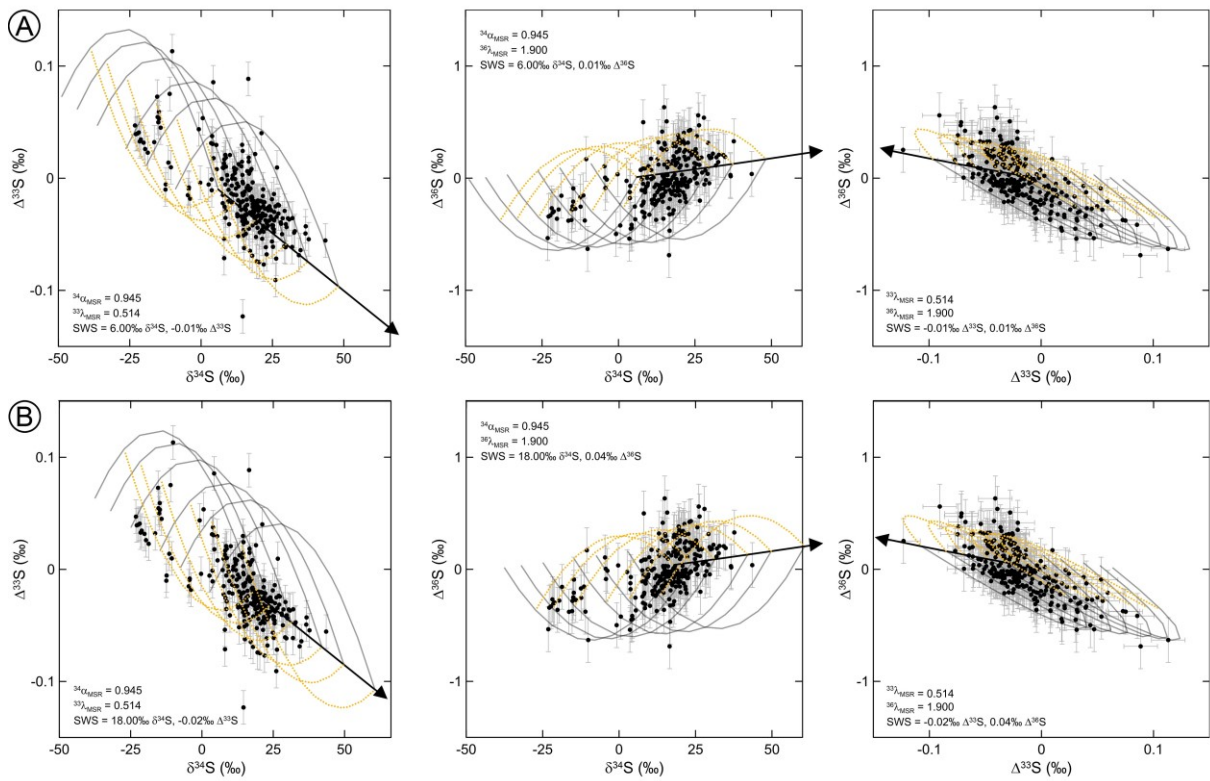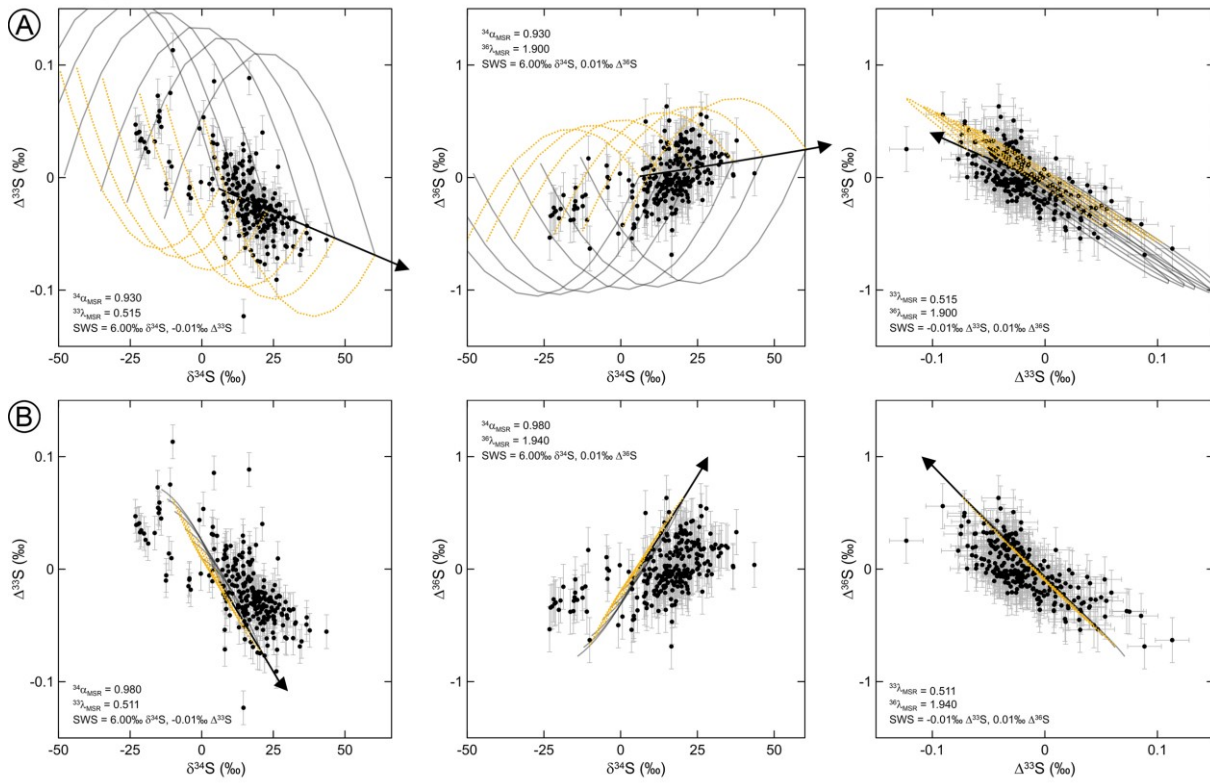668 Member B and Member C, respectively.
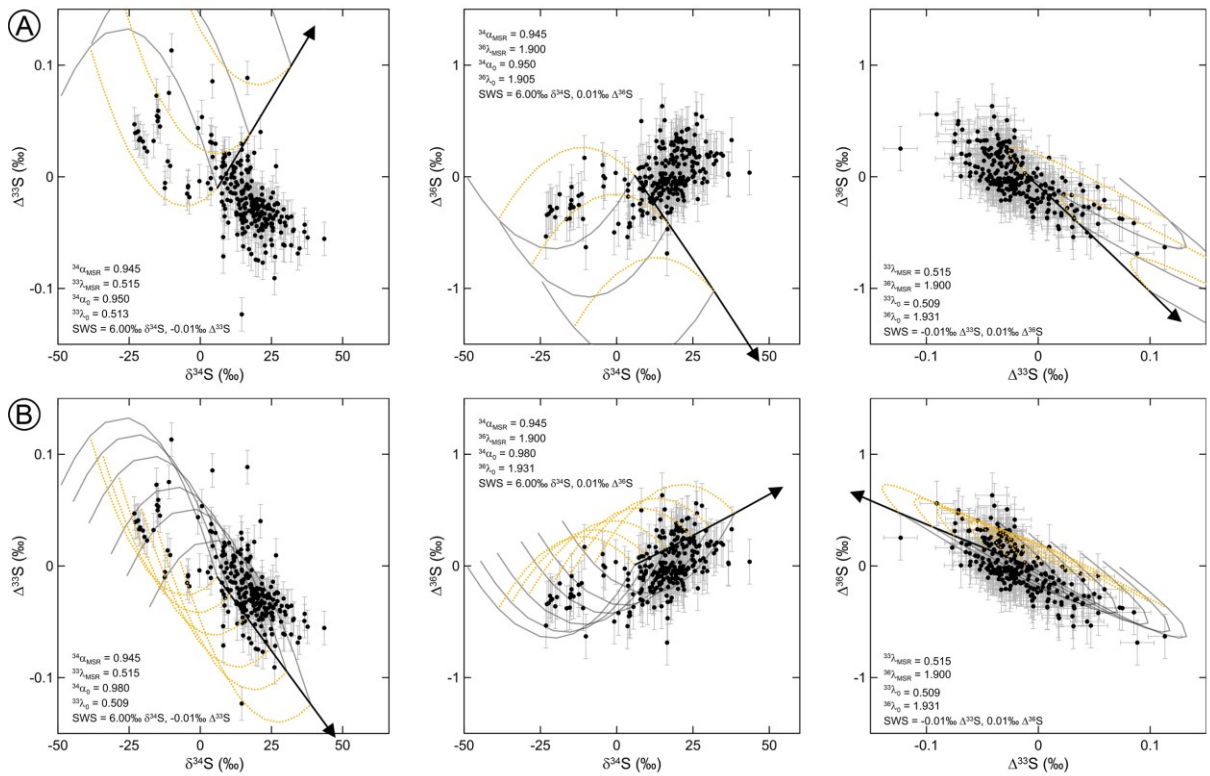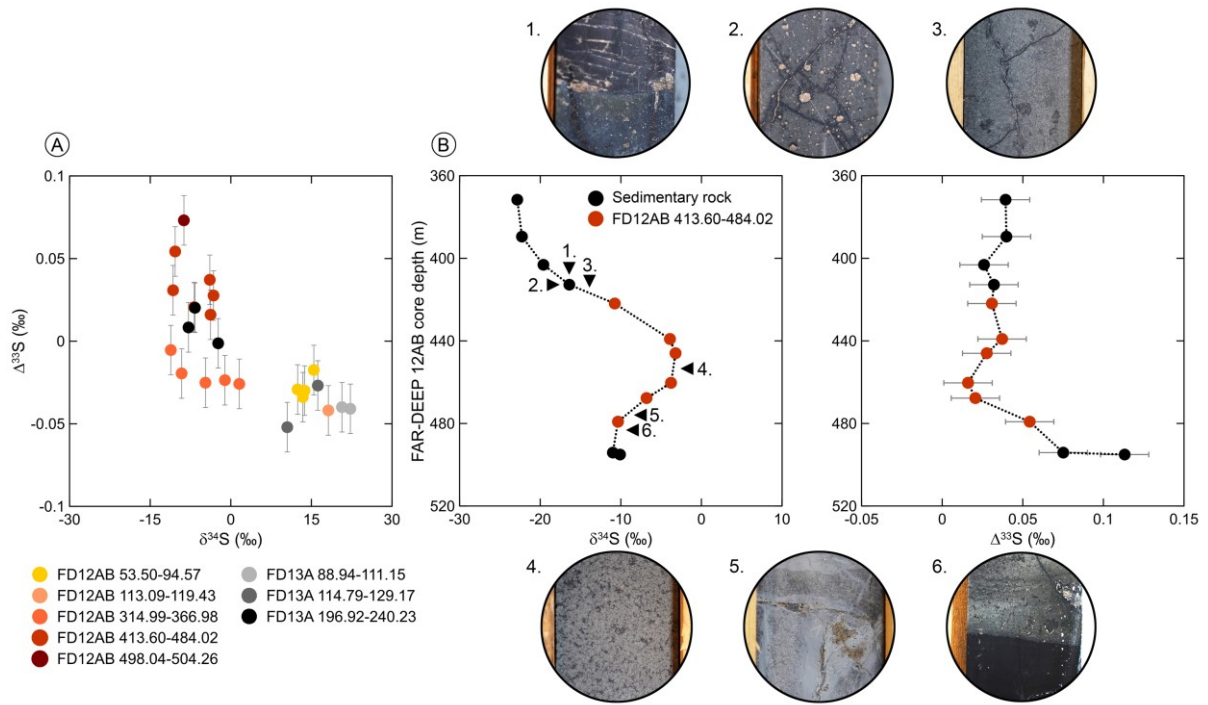
669

670   Figure 1
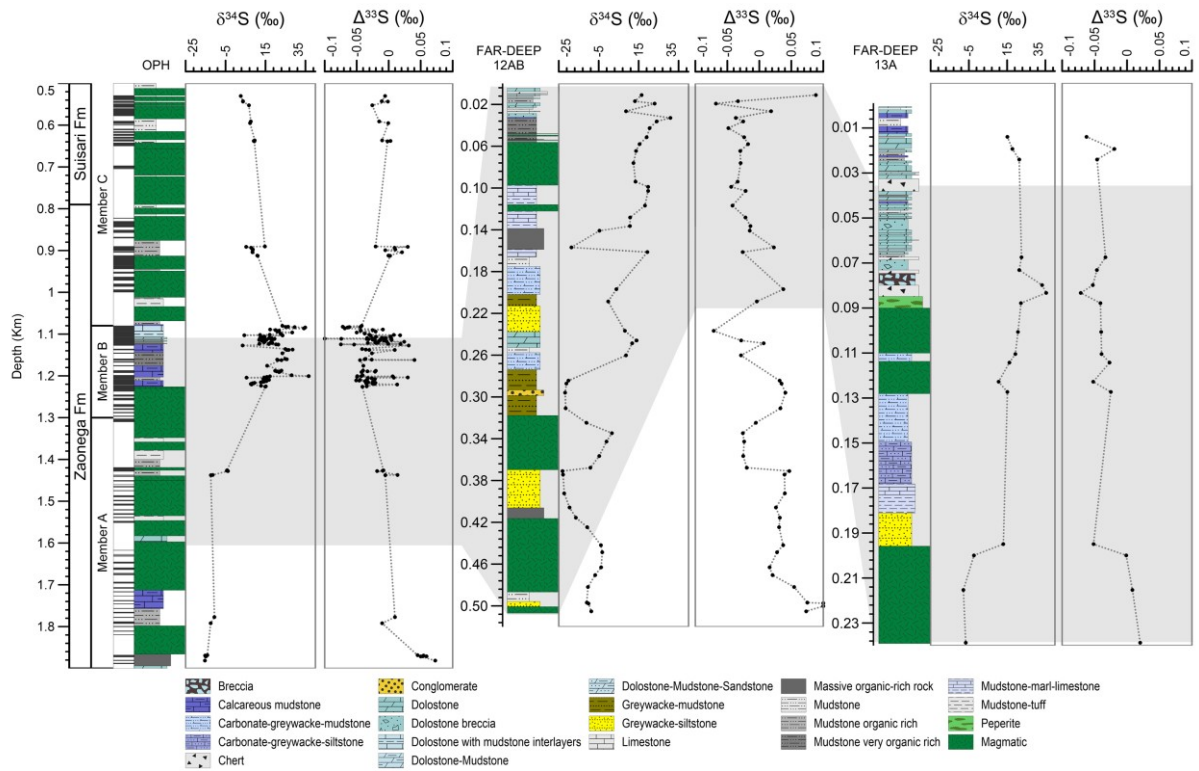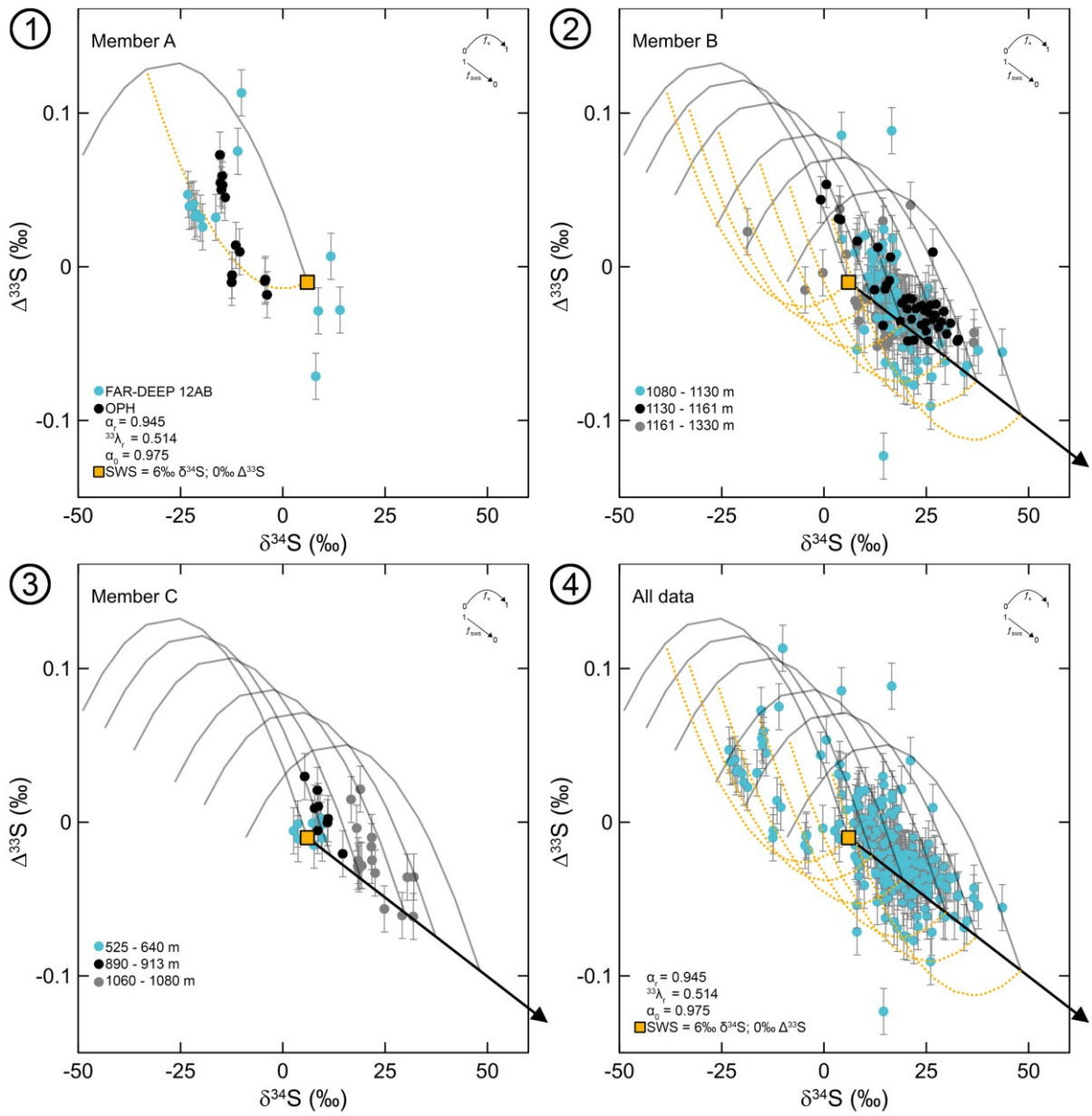

671

672   Figure 2

673

674   Figure 3

675

676   Figure 4
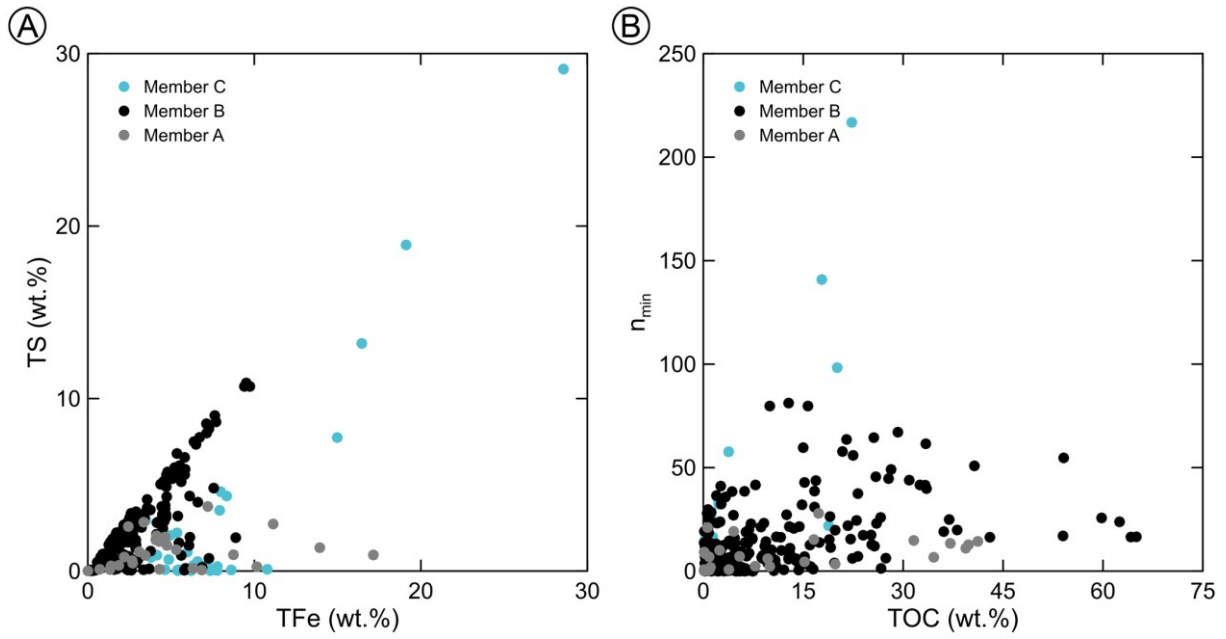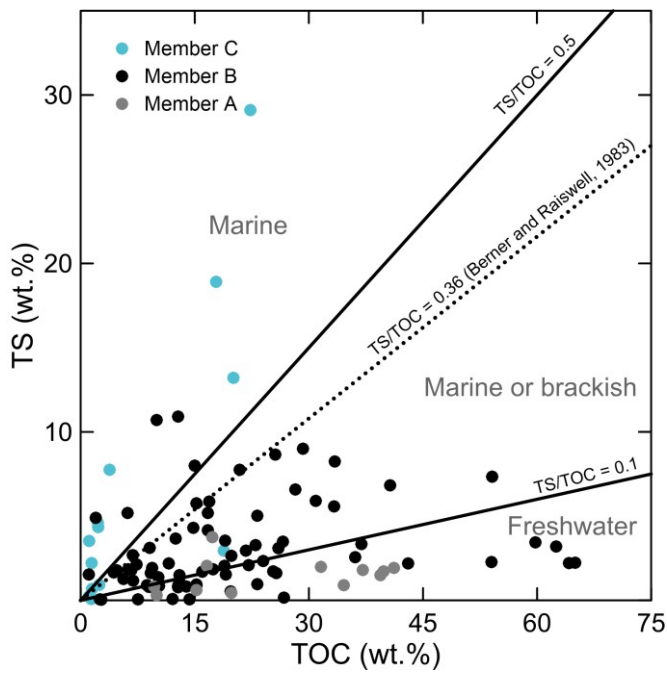

677

678   Figure 5

679

680

681   Figure 6

682

683

684   Figure 7

685

686

687   Figure 8

688

689

690

Appendix A

### 1. Materials

We integrate bulk pyrite sulphur isotope and major element data of several drill cores from three different locations in the Onega Basin (Fig. 1) that include new data from the Onega Parametric Hole (OPH, 119 samples), FAR-DEEP 12AB (49 samples) and 13A (17 samples) cores and published data from the OnZap cores (Paiste et al., 2018). Detailed descriptions of the OPH, FAR-DEEP and OnZap cores are available in Krupenik et al. (2011), Črne et al. (2013a,b) and Paiste et al. (2018), respectively.

Cores from all studied locations can be correlated using a basin-scale massive dolomite unit in the upper part of the Zaonega Formation (Črne et al., 2013a,b; Melezhik et al., 2015; Paiste et al., 2018; Qu et al., 2012) which is characterized by infrequent intervals of up to 1 cm thick discontinuous apatite layers at its base (Joosu et al., 2015; Lepland et al., 2014). The dolomite unit is cut by distinct black silica veins that can be several meters thick and contain relicts of the dolomite. These veins typically follow thin mudstone layers within the dolomite whereas their thickness and frequency vary at different sites. Despite such alteration the massive dolostone unit is readily identified in all cores and serves as a basin-scale lithostratigraphic marker.

The Zaonega Formation in the correlated succession has been subdivided into three Members-A, B and C (Fig. A.1). Using the OPH core as a reference, Member A comprises the depth intervals at 2115–1330 in the OPH core and 504–234 m in FAR-DEEP 12AB core. Member B is assigned to the intervals at 1330–1080 m in the OPH, 234–1.6 m in the FAR-DEEP 12AB, 240–14 m in FAR-DEEP 13A cores and 102–21 m in the OnZap section. Member C includes the intervals at 1080–528 m in the OPH core (the upper part of the Zaonega Formation and the

lower part of the overlaying Suisari Formation), 14–1.6 m in FAR-DEEP 13A core and 21–1.7 m in the OnZap section.
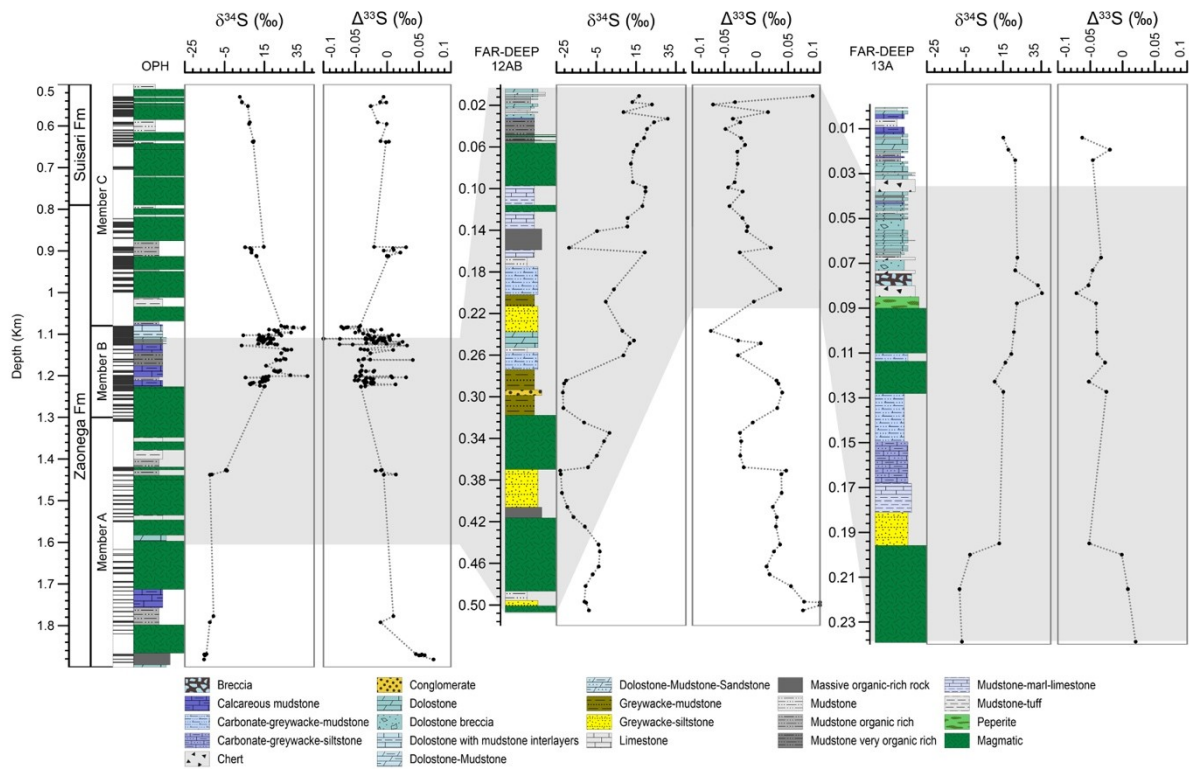
Figure A.1. Lithostratigraphic profiles and new $\delta^{34}S$ and $\Delta^{33}S$ data from the OPH, FAR-DEEP 12AB and 13A cores. These data are used to divide the OPH core into Members A, B and C (see text for details). A basin-scale massive dolomite unit is used for correlation between drill cores and stratigraphic intervals displaying similar isotope records are highlighted in grey. Black bars at the side of the OPH lithological profile represent intervals of core recovery; interpolation of rock types in zones of no recovery are based on interpretations of downhole geophysical data (after Morozov et al. 2010).

2. Simulation of the sulfur isotope record in the Zaonega Formation

2.1 Open vs closed system

In order to estimate if the reduced sulfur in sediments was formed in a setting open to sulfate transport the minimum number of pore volumes was calculated according to:

31

728    $n_{min} = c_{sed} * \rho * (1-\eta) / c_{sw} \eta$, (Eq. A.1)

729   where c_{sed} (g S/g sediment) is the total reduced sedimentary sulfur for each sample, ρ is the

730   density of sedimentary solids (g/cm^3), η is the initial sediment porosity ($0 < \eta < 1$) and c_{sw} (g

731   S/cm^3) is the concentration of seawater sulfate (Zaback et al., 1993). The n_{min} indicates the

732   number of pore volumes with given seawater sulfate concentration that was required to produce

733   the total sulfur preserved in the sediment. A ρ of 2.15 g/cm^3 and η was set at 0.9 assuming an

734   unconsolidated organic-rich pelagic mud. It is acknowledged that the fixed parameters ρ and η

735   are difficult to estimate and may have varied between lithologies. However, these determine

736   the magnitude of n_{min} values and even by using very high or low input parameters the general

737   trends remain unchanged. Seawater sulfate concentrations were constrained at 10 mM as has

738   been determined for the underlying Tulomozero Formation (Blättler et al., 2018). We notice

739   that lower porosity and/or lower sweater sulfate levels would result in respective increases in

740   n_{min} values and the calculated values represent a reasonable minimum.

741   **2.2 Sulfur fluxes and sulfur isotope fractionation**

742   The sulfur isotope signatures preserved in the Zaonega Formation can be replicated by

743   constructing three sulfur reservoirs; seawater sulfate ($SO_4^{2-}{}_{SW}$), pore water sulfate ($SO_4^{2-}{}_{PW}$)

744   and unretained sulfide (HS$^-$). Sulfur is exchanged between these reservoirs. The fluxes of sulfur

745   along a given pathway are defined as ϕ_1 = sulfate entering from the water column, ϕ_2 = microbial

746   sulfate reduction, ϕ_3 = sulfide captured in sediment, ϕ_4 = sulfide oxidation and ϕ_5 = sulfate

747   returned to the water column (Fig. A.3). This steady-state model approach was developed by

748   Zaback et al. (1993) and modified to accommodate the multiple sulfur isotope system. For a

749   specific pathway (i):

750    $\delta^{3x}S_i = 1000 \cdot ({}^{3x}R_i / {}^{3x}R_{V\text{-}CDT} - 1)$, (Eq. A.2)

751   where ${}^{3x}R_i = {}^{3x}S/{}^{32}S$, for 3x = 33, 34 or 36. The $\Delta^{33}S$ and $\Delta^{36}S$ are calculated accordingly:

752     $\Delta^{3x}S = \delta^{3x}S - 1000 \cdot [(1 + \delta^{34}S/1000)^{3x\lambda} - 1]$, (Eq. A.3)

753   where $3x = 33$ or 36, $^{33}\lambda = 0.515$ and $^{36}\lambda = 1.9$.

754   At steady state, the flux of sulfur in and out of the sediment will be equal in quantity (ϕ_i) and

755   isotope composition ($\delta^{3x}S_i$) according to mass balance:

756     $\phi_1\delta^{3x}S_1 + \phi_4\delta^{3x}S_4 = \phi_5\delta^{3x}S_5 + \phi_2\delta^{3x}S_2$, (Eq. A.4)

757   and the unretained sulfide pool has to be balanced by the fluxes of sulfur oxidized and removed

758   as reduced sulfur from the system:

759     $\phi_2\delta^{3x}S_2 = \phi_3\delta^{3x}S_3 + \phi_4\delta^{3x}S_4$. (Eq. A.5)

760   The distribution of material along a given pathway and related isotope effects govern isotope

761   fractionations within the system and those associated with sulfate transport can be described

762   accordingly:

763     $^{3x}\alpha_t = (1000+\delta^{3x}S_{SO4\,SW})/(1000+\delta^{3x}S_1) = (1000+\delta^{3x}S_{SO4\,PW})/(1000+\delta^{3x}S_5)$, (Eq. A.6)

764   and for microbial sulfate reduction:

765     $^{3x}\alpha_{MSR} = (1000+\delta^{3x}S_{SO4\,PW})/(1000+\delta^{3x}S_2)$. (Eq. A.7)

766   For ^{33}S and ^{36}S the following mass dependent relationships apply (Ono et al., 2006):

767     $^{33}\alpha = {}^{34}\alpha^{33\lambda}$ (Eq. A.8)

768   and,

769     $^{36}\alpha = {}^{34}\alpha^{36\lambda}$ (Eq. A.9)

770   It has been demonstrated that both abiotic and biological sulfide oxidation can be accompanied

771   by small <5‰ fractionations for $\delta^{34}S$ (Balci et al., 2007; Fry et al., 1988; Kaplan and Rittenberg,

772   1964; Zerkle et al., 2009) and experimental studies have reported <0.1‰ $\Delta^{33}S$ and <0.9‰ $\Delta^{36}S$

773 fractionations from pure culture studies (Zerkle et al., 2009), however, these are not well known

774 for natural communities. Since, the main focus of this study is on the reductive part of the sulfur

775 cycle, it is assumed that no isotope effects are associate with the branching of sulfur along

776 pathways ϕ_3 and ϕ_4. According to mass balance the $\delta^{3x}S_2$, $\delta^{3x}S_3$, $\delta^{3x}S_4$ and $\delta^{3x}S_{PY}$ (reduced

777 sedimentary sulfide) will be all equal and the overall fractionation factor can be determined as

778 follows:

779 $^{3x}\alpha_0 = f_s \cdot {}^{3x}\alpha_t + (1 - f_s) \, {}^{3x}\alpha_{MSR}$, (Eq. A.10)

780 where $f_s = \phi_3/\phi_1$ is the fraction of imported sulfate that was removed from the system as reduced

781 sulfur and $(1 - f_s)$ is the residual sulfate. Assuming that $^{3x}\alpha_t = 1$, then $^{3x}\alpha_0 = (1000+\delta^{3x}S_{SO4}$

782 $_{SW})/(1000+\delta^{3x}S_{PY})$.

2.3 Model parameters

784 For the input parameters α_{MSR} was set at 0.945, $^{33}\lambda_{MSR}$ of 0.514 was calculated from the slope

785 determined by the regression of $\Delta^{33}S$ vs. $\delta^{34}S$ plot for MSR (Kunzmann et al., 2017; Pellerin et

786 al., 2015; Sim et al., 2011) and a $^{36}\lambda_{MSR}$ equal to 1.91 was taken from reported culture

787 experiments (Aoyama et al., 2014; Johnston et al., 2008, 2007, 2005). The lower compositional

788 limit for SWS was derived from the lower lying Tulomozero Formation and set at 6‰ $\delta^{34}S$, -

789 0.01‰ $\Delta^{33}S$ and 0.01‰ $\Delta^{36}S$ (Blättler et al., 2018). An upper estimate inferred in a similar way

790 as in Scott et al. (2014) from pyrite sulfur isotope data suggests $\delta^{34}S_{SWS}$ of 18‰, $\Delta^{33}S_{SWS}$ of -

791 0.02‰ and $\Delta^{36}S_{SWS}$ of 0.04‰ could represent the ambient sulfate isotopic composition during

792 deposition of the upper Zaonega Formation (Fig. A.2).
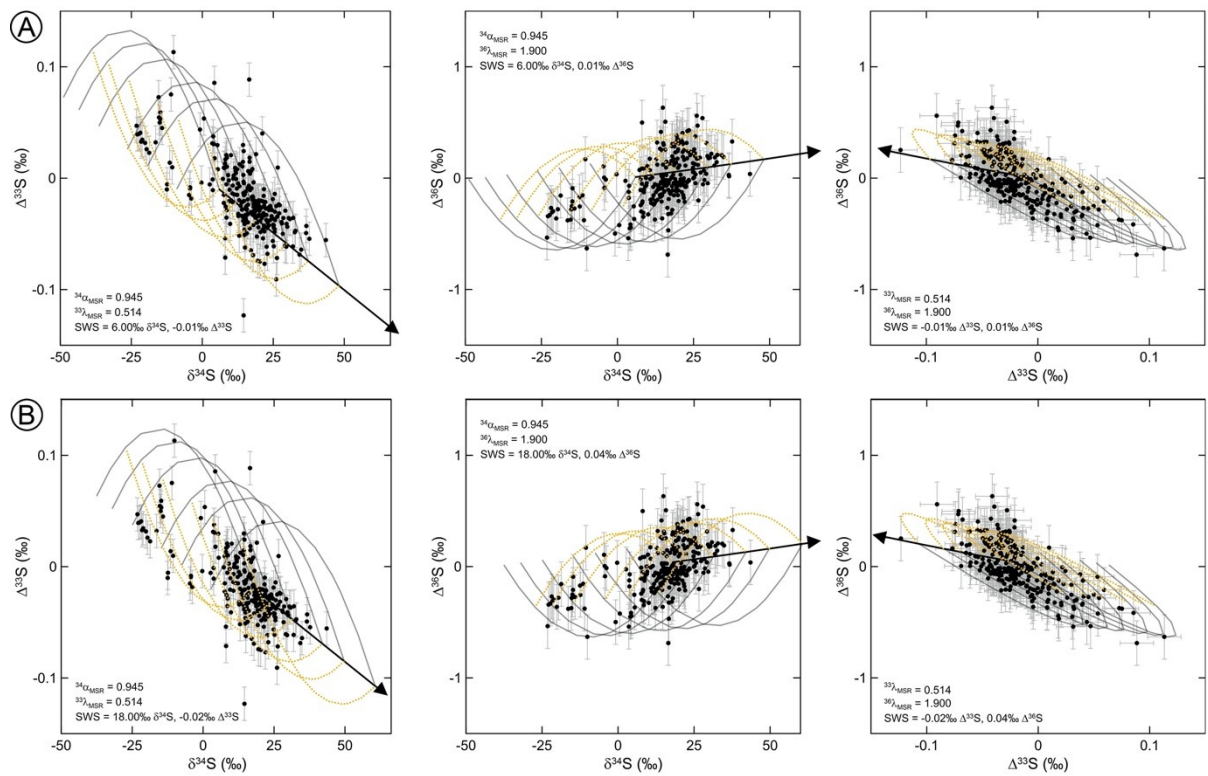
Figure A.2. Sensitivity test results for variable seawater sulfate (SWS) isotope composition A. $\delta^{34}S$ = 6‰, $\Delta^{33}S$ = -0.01‰ and $\Delta^{36}S$ = 0.01‰ (taken from Blättler et al., 2018) and B. SWS $\delta^{34}S$ = 18‰, $\Delta^{33}S$ = -0.02‰, $\Delta^{36}S$ = 0.04‰ (inferred from pyrite data). Grey curved lines display vectors for modelled pyrite $\Delta^{33}S$-$\delta^{34}S$ pairs that formed from sulfate with an isotope composition at the right end of the curve. Black line represents the trajectory for Rayleigh fractionation of SWS and the yellow dotted curved line mixing between two sulfide endmembers, where one formed in open-system and the other in closed-system conditions.

2.5 Rayleigh fractionation of the basinal sulfate reservoir

In order to explore the effects of basinal restriction on the produced sulfide, the seawater sulfate isotope composition was allowed to evolve as a result of a contraction of the sulfate reservoir and corresponding Rayleigh distillation resulting from the preferential consumption of lighter isotopes of sulfur by sulfate reduction. The isotope mass balance model for sedimentary sulfides assumes that a constant flux of sulfate with a given isotope composition was imported into the sediments. However, if basinal sulfate concentrations decrease, it is possible that open system

808   conditions describe the sedimentary environment but that the basinal sulfate evolves according

809   to Rayleigh distillation:

810    $^{3x}R_0 = {}^{3x}R_{fsws} * (f_{sws})^{(3x\alpha 0-1)}$, (Eq. A.11)

811   where $^{3x}R = {}^{3x}S/{}^{32}S$, for 3x = 33, 34 or 36, $^{3x}\alpha_0$ is the net fractionation factor for every isotope

812   and f_{sws} is the fraction of sulfate remaining in the basinal sulfate reservoir after a portion of

813   sulfate has been reduced by MSR and buried as reduced sulfur. The net fractionation factors

814   were derived from the steady-state model for sulfide according to Eq. A.10 and set at $^{34}\alpha_0$ 0.974,

815    $^{33}\lambda_0$ 0.510 and $^{36}\lambda_0$ 1.926, assuming f_s of 0.55.

816   ## 3. Sensitivity test

817   In order to explore the effects of variations in α_{MSR} and α_0, additional sensitivity tests were

818   performed (Fig. A.3) by using the same initial seawater sulfate composition (-0.01‰ Δ^{33}S, 6‰

819   δ^{34}S and 0.01‰ Δ^{36}S) and varying the paired $^{33}\lambda$ and $^{36}\lambda$ depending on the chosen $^{34}\alpha_{MSR}$ as

820   has been determined from pure culture studies of sulfate reducers (Aoyama et al., 2014;

821   Johnston et al., 2008, 2007, 2005). A span of $^{34}\alpha_{MSR}$ values between 0.93–0.98 could also

822   reproduce a large part of the observed pyrite compositions (Fig. A.3). However, a high

823   fractionation factor ($^{34}\alpha_{MSR}$ >0.98) implies lower f_s values and more open-system conditions.

824   Low f_s values would impart only a limited effect on the basinal sulfate isotope composition that

825   is not consistent with the proposed Rayleigh distillation of seawater sulfate. The maximum

826   observed fractionation for MSR ($^{34}\alpha_{MSR}$ = 0.93) would produce a very large model field but

827   implies $f_s \rightarrow 1$ indicating no fractionation between seawater sulfate and sulfide which would

828   not have any significant impact on the basinal pool. Even though a range of possible $^{34}\alpha_{MSR}$

829   values between 0.93–0.98 could reproduce the observed pyrite record, they all imply high

830   values of f_s and that other factors such as organic carbon loading or sedimentary processes were

831   governing the sulfate transport. Therefore, $^{34}\alpha_{MSR}$ between 0.93–0.98 do not change our

832   interpretation and $^{34}\alpha_{MSR}$ of 0.945 serves as a reasonable estimate.

833
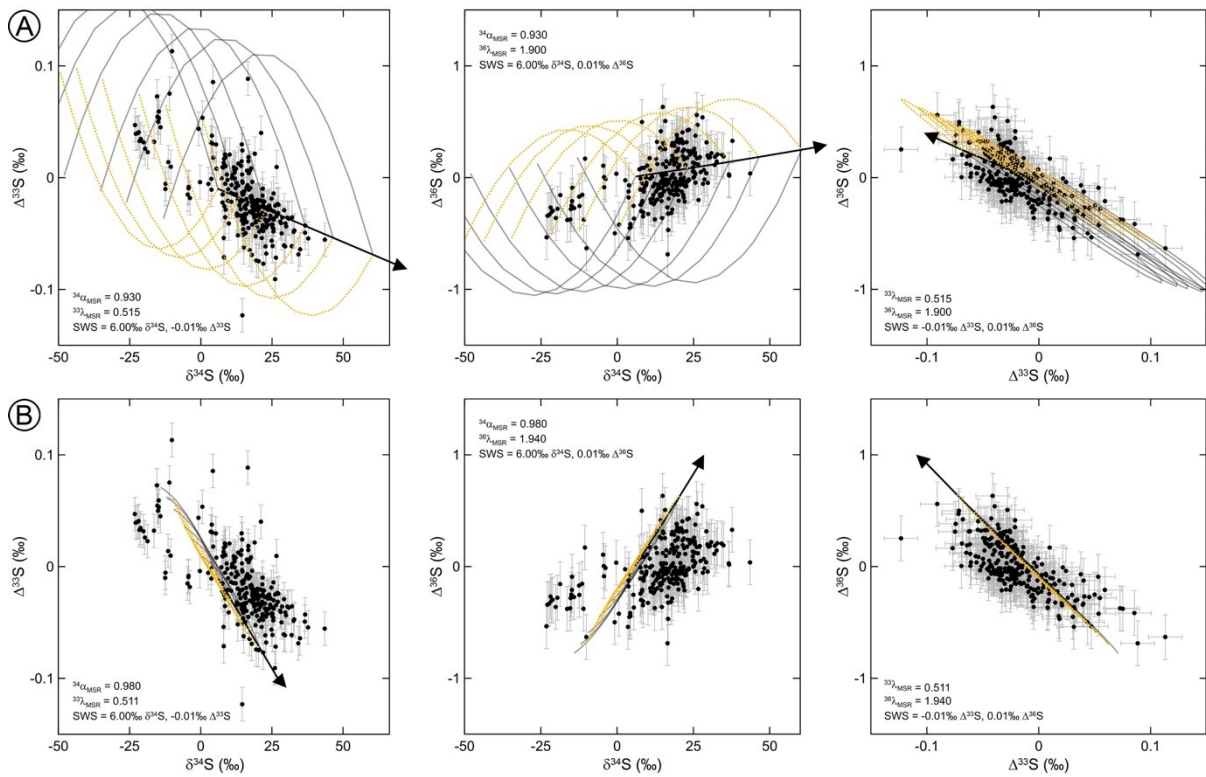
Figure A.3. Sensitivity test results for variations in microbial fractionation factors and its effects on net fractionation factors if $f_s = 0.55$ and initial SWS is $\delta^{34}S = 6‰$, $\Delta^{33}S = -0.01‰$ and $\Delta^{36}S = 0.1‰$. A. $^{34}\alpha_{MSR} = 0.93$, $^{33}\lambda_{MSR} = 0.515$, $^{36}\lambda_{MSR} = 1.90$ and B. $^{34}\alpha_{MSR} = 0.98$, $^{33}\lambda_{MSR} = 0.511$, $^{36}\lambda_{MSR} = 1.94$. Grey curved lines display vectors for modelled pyrite $\Delta^{33}S$-$\delta^{34}S$ pairs that formed from sulfate with an isotope composition at the right end of the curve. Black line represents the trajectory for Rayleigh fractionation of SWS and the yellow dotted curved line mixing between two sulfide endmembers, where one formed in open-system and the other in closed-system conditions.

842   The net fractionation factor depends on the $^{34}\alpha_{MSR}$ and f_s values, which in turn influence the

843   basinal sulfate reservoir only if $\alpha_{MSR} > \alpha_0 < 1$. Accordingly, the set of model predictions for the

844   Zaonega Formation sulfides suggest $^{34}\alpha_0$ values from 0.974 paired with $^{33}\lambda_0$ of 0.510 and $^{36}\lambda_0$

845   of 1.926 to $^{34}\alpha_0$ 0.995, $^{33}\lambda_0$ of 0.507 and $^{36}\lambda_0$ of 1.955 (Fig. A.4). Inserting $^{34}\alpha_0$ values below

846   0.975 and accordingly $^{33}\lambda_0$ above 0.510 ($^{36}\lambda_0$<1.926) to the Rayleigh equation produce model

847   fields that do not follow the observed trends in measured pyrite δ^{34}S data, whereas $^{34}\alpha_0$ greater

848   than 0.980, $^{33}\lambda_0$<0.508 and $^{36}\lambda_0$>1.950 would generate very narrow model fields that do not

849   reproduce a large part of the pyrite compositions. It is possible that the addition of substrates in

850   Member B increased rates of organic matter mineralisation that could result in greater $^{34}\alpha_0$ and

851   smaller $^{33}\lambda_0$ values. However, the relatively constant range of f_s values in the lower part of

852   Member B suggests that even if the net fractionation factors varied an $^{34}\alpha_0$ of 0.975, $^{33}\lambda_0$ of

853   0.510 and $^{36}\lambda_0$ of 1.926 are reasonable and constant with the observed sulfide trends.

854
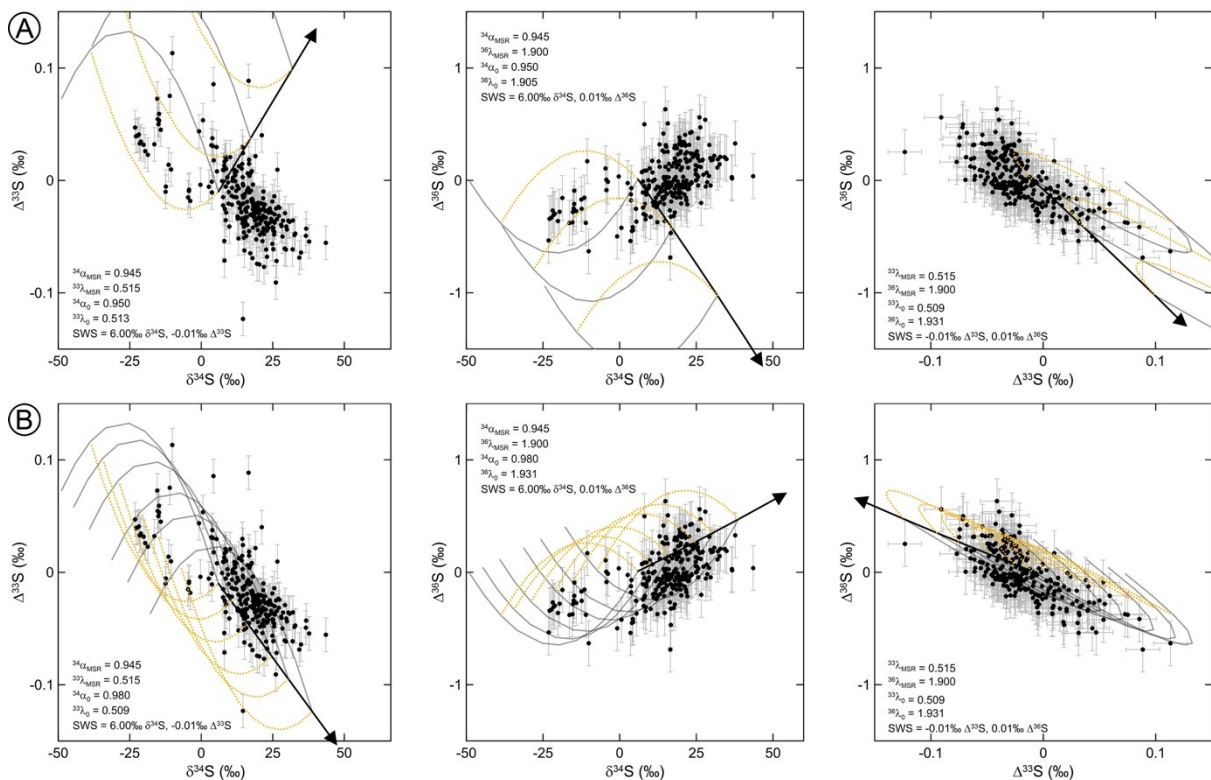
Figure A.4. Sensitivity test results for variable net fractionation factors at an initial SWS of

δ^{34}S = 6‰, Δ^{33}S = -0.01 and Δ^{36}S = 0.01‰ and constant microbial fractionations ($^{34}\alpha_{MSR}$ =

0.945, $^{33}\lambda_{MSR}$ = 0.514, $^{36}\lambda_{MSR}$ = 1.90). A. $^{34}\alpha_0$ = 0.95, $^{33}\lambda_0$ = 0.513, $^{36}\lambda_0$ = 1.91 and B. $^{34}\alpha_0$ =

0.98, $^{33}\lambda_0$ = 0.509, $^{36}\lambda_0$ = 1.93. Grey curved lines display vectors for modelled pyrite Δ^{33}S-δ^{34}S

pairs that formed from sulfate with an isotope composition at the right end of the curve. Black line represents the trajectory for Rayleigh fractionation of SWS and the yellow dotted curved line mixing between two sulfide endmembers, where one formed in open-system and the other in closed-system conditions.

Table caption

Table A.1. Sulphur, carbon and iron content, pyrite multiple sulfur isotope data of whole rock samples and calculated n_{min} values for the FAR-DEEP 12AB, FAR-DEEP 13A and OPH drill cores from the Zaonega Formation, Onega Basin, NW Russia. The reported n_{min} values were calculated at given (2 mM, 10 mM and 28 mM) seawater sulfate concentrations.

References

Aoyama, S., Nishizawa, M., Takai, K., Ueno, Y., 2014. Microbial sulfate reduction within the Iheya North subseafloor hydrothermal system constrained by quadruple sulfur isotopes. Earth Planet Sc Lett 398, 113–126. https://doi.org/10.1016/j.epsl.2014.04.039

Balci, N., Shanks, W.C., Mayer, B., Mandernack, K.W., 2007. Oxygen and sulfur isotope systematics of sulfate produced by bacterial and abiotic oxidation of pyrite. Geochimica et Cosmochimica Acta 71, 3796–3811. https://doi.org/10.1016/j.gca.2007.04.017

Blättler, C.L., Claire, M.W., Prave, A.R., Kirsimäe, K., Higgins, J.A., Medvedev, P.V., Romashkin, A.E., Rychanchik, D.V., Zerkle, A.L., Paiste, K., Kreitsmann, T., Millar, I.L., Hayles, J.A., Bao, H., Turchyn, A.V., Warke, M.R., Lepland, A., 2018. Two-billion-year-old evaporites capture Earth's great oxidation. Science eaar2687. https://doi.org/10.1126/science.aar2687

Črne, A.E., Melezhik, V.A., Prave, A.R., Lepland, A., Romashkin, A.E., Rychanchik, D.V., Hanski, E.J., Luo, Z., 2013a. Zaonega Formation: FAR-DEEP Holes 12A and 12B, and Neighbouring quarries, in: Melezhik, V.A., Prave, A.R., Fallick, A.E., Hanski, E.J., Lepland, A., Kump, L.R., Strauss, H. (Eds.), Reading the Archive of Earth's Oxygenation: Volume 2: The Core Archive of the Fennoscandian Arctic Russia - Drilling Early Earth Project, Frontiers in Earth Sciences. Springer, pp. 946–1007.

Črne, A.E., Melezhik, V.A., Prave, A.R., Lepland, A., Romashkin, A.E., Rychanchik, D.V., Hanski, E.J., Luo, Z., 2013b. Zaonega Formation: FAR-DEEP Hole 13A, in: Melezhik, V.A., Prave, A.R., Fallick, A.E., Hanski, E.J., Lepland, A., Kump, L.R., Strauss, H. (Eds.), Reading the Archive of Earth's Oxygenation: Volume 2: The Core Archive of the Fennoscandian Arctic Russia - Drilling Early Earth Project, Frontiers in Earth Sciences. Springer, pp. 1008–1046.

Fry, B., Ruf, W., Gest, H., Hayes, J.M., 1988. Sulfur isotope effects associated with oxidation of sulfide by O2 in aqueous solution. Chemical Geology: Isotope Geoscience section 73, 205–210. https://doi.org/10.1016/0168-9622(88)90001-2

Johnston, D.T., Farquhar, J., Canfield, D.E., 2007. Sulfur isotope insights into microbial sulfate reduction: When microbes meet models. Geochimica et Cosmochimica Acta 71, 3929–3947. https://doi.org/DOI 10.1016/j.gca.2007.05.008

Johnston, D.T., Farquhar, J., Habicht, K.S., Canfield, D.E., 2008. Sulphur isotopes and the search for life: strategies for identifying sulphur metabolisms in the rock record and beyond. Geobiology 6, 425–435. https://doi.org/10.1111/j.1472-4669.2008.00171.x

Johnston, D.T., Farquhar, J., Wing, B.A., Kaufman, A., Canfield, D.E., Habicht, K.S., 2005. Multiple sulfur isotope fractionations in biological systems: A case study with sulfate reducers and sulfur disproportionators. Am J Sci 305, 645–660. https://doi.org/DOI 10.2475/ajs.305.6-8.645

Joosu, L., Lepland, A., Kirsimae, K., Romashkin, A.E., Roberts, N.W., Martin, A.P., Crne, A.E., 2015. The REE-composition and petrography of apatite in 2 Ga Zaonega Formation, Russia: The environmental setting for phosphogenesis. Chemical Geology 395, 88–107. https://doi.org/10.1016/j.chemgeo.2014.11.013

Kaplan, I.R., Rittenberg, S.C., 1964. Microbiological Fractionation of Sulphur Isotopes. Microbiology 34, 195–212. https://doi.org/10.1099/00221287-34-2-195

Krupenik, V.A., Akhmedov, A.M., Sveshnikova, K.Y., 2011. Isotopic composition of carbon, oxygen and sulfur in the Ludicovian and Jatulian rocks, in: Glushanin, L.V., Sharov, N.V., Shchiptsov, V.V. (Eds.), The Onega Paleoproterozoic Structure (Geology, Tectonics, Deep Structure, Minerogeny). Institute of Geology, Karelian Research Centre RAS, Petrozavodsk, pp. 250–255.

Kunzmann, M., Bui, T.H., Crockford, P.W., Halverson, G.P., Scott, C., Lyons, T.W., Wing, B.A., 2017. Bacterial sulfur disproportionation constrains timing of Neoproterozoic oxygenation. Geology 45, 207–210. https://doi.org/10.1130/G38602.1

Lepland, A., Joosu, L., Kirsimae, K., Prave, A.R., Romashkin, A.E., Crne, A.E., Martin, A.P., Fallick, A.E., Somelar, P., Upraus, K., Mand, K., Roberts, N.M.W., van Zuilen, M.A., Wirth, R., Schreiber, A., 2014. Potential influence of sulphur bacteria on Palaeoproterozoic phosphogenesis. Nat Geosci 7, 20–24. https://doi.org/10.1038/Ngeo2005

Melezhik, V.A., Fallick, A.E., Brasier, A.T., Lepland, A., 2015. Carbonate deposition in the Palaeoproterozoic Onega basin from Fennoscandia: a spotlight on the transition from the Lomagundi-Jatuli to Shunga events. Earth-Sci Rev 147, 65–98. https://doi.org/10.1016/j.earscirev.2015.05.005

Morozov, A.F., Hakhaev, B.N., Petrov, O.V., Gorbachev, V.I., Tarkhanov, G.B., Tsvetkov, L.D., Erinchek, Y.M., Akhmedov, A.M., Krupenik, V.A., Sveshnikova, K.Y., 2010. Rock-salts in Palaeoproterozoic strata of the Onega depression of Karelia (based on data from the Onega parametric drillhole). Transection of Academy of Sciences 435, 230–233.

Ono, S., Wing, B., Johnston, D., Farquhar, J., Rumble, D., 2006. Mass-dependent fractionation of quadruple stable sulfur isotope system as a new tracer of sulfur biogeochemical cycles. Geochimica et Cosmochimica Acta 70, 2238–2252. https://doi.org/DOI 10.1016/j.gca.2006.01.022

Paiste, K., Lepland, A., Zerkle, A.L., Kirsimäe, K., Izon, G., Patel, N.K., McLean, F., Kreitsmann, T., Mänd, K., Bui, T.H., Romashkin, A.E., Rychanchik, D.V., Prave, A.R., 2018. Multiple sulphur isotope records tracking basinal and global processes in the 1.98 Ga Zaonega Formation, NW Russia. Chemical Geology 499, 151–164. https://doi.org/10.1016/j.chemgeo.2018.09.025

Pellerin, A., Bui, T.H., Rough, M., Mucci, A., Canfield, D.E., Wing, B.A., 2015. Mass-dependent sulfur isotope fractionation during reoxidative sulfur cycling: A case study from Mangrove Lake, Bermuda. Geochimica et Cosmochimica Acta 149, 152–164. https://doi.org/10.1016/j.gca.2014.11.007

Qu, Y., Crne, A.E., Lepland, A., Van Zuilen, M.A., 2012. Methanotrophy in a Paleoproterozoic oil field ecosystem, Zaonega Formation, Karelia, Russia. Geobiology 10, 467–478. https://doi.org/Doi 10.1111/Gbi.12007

Sim, M.S., Bosak, T., Ono, S., 2011. Large Sulfur Isotope Fractionation Does Not Require Disproportionation. Science 333, 74–77. https://doi.org/10.1126/science.1205103

Zaback, D.A., Pratt, L.M., Hayes, J.M., 1993. Transport and reduction of sulfate and immobilization of sulfide in marine black shales. Geology 21, 141–144. https://doi.org/10.1130/0091-7613(1993)021<0141:TAROSA>2.3.CO;2

Zerkle, A.L., Farquhar, J., Johnston, D.T., Cox, R.P., Canfield, D.E., 2009. Fractionation of multiple sulfur isotopes during phototrophic oxidation of sulfide and elemental sulfur by a green sulfur bacterium. Geochimica et Cosmochimica Acta 73, 291–306. https://doi.org/10.1016/j.gca.2008.10.027